

Air Force Institute of Technology

AFIT Scholar

Theses and Dissertations

Student Graduate Works

3-22-2007

CFD Investigation of Flow Past Idealized Engine Nacelle Clutter /// Computational fluid dynamics investigation of flow past idealized engine nacelle clutter

Matthew S. Caspers

Follow this and additional works at: <https://scholar.afit.edu/etd>



Part of the [Aerodynamics and Fluid Mechanics Commons](#)

Recommended Citation

Caspers, Matthew S., "CFD Investigation of Flow Past Idealized Engine Nacelle Clutter /// Computational fluid dynamics investigation of flow past idealized engine nacelle clutter" (2007). *Theses and Dissertations*. 2962.

<https://scholar.afit.edu/etd/2962>

This Thesis is brought to you for free and open access by the Student Graduate Works at AFIT Scholar. It has been accepted for inclusion in Theses and Dissertations by an authorized administrator of AFIT Scholar. For more information, please contact richard.mansfield@afit.edu.



CFD INVESTIGATION OF FLOW PAST
IDEALIZED ENGINE NACELLE CLUTTER

THESIS

Matthew S. Caspers, Captain, USAF

AFIT/GAE/ENY/07-M08

DEPARTMENT OF THE AIR FORCE
AIR UNIVERSITY

AIR FORCE INSTITUTE OF TECHNOLOGY

Wright-Patterson Air Force Base, Ohio

APPROVED FOR PUBLIC RELEASE; DISTRIBUTION UNLIMITED.

The views expressed in this thesis are those of the author and do not reflect the official policy or position of the United States Air Force, Department of Defense, or the United States Government.

AFIT/GAE/ENY/07-M08

CFD INVESTIGATION OF FLOW PAST
IDEALIZED ENGINE NACELLE CLUTTER

THESIS

Presented to the Faculty

Department of Aeronautics and Astronautics Engineering

Graduate School of Engineering and Management

Air Force Institute of Technology

Air University

Air Education and Training Command

In Partial Fulfillment of the Requirements for the
Degree of Master of Science in Aeronautical Engineering

Matthew S. Caspers, B.S.

Captain, USAF

March 2007

APPROVED FOR PUBLIC RELEASE; DISTRIBUTION UNLIMITED.

CFD INVESTIGATION OF FLOW PAST
IDEALIZED ENGINE NACELLE CLUTTER

Matthew S. Caspers, B.S.
Captain, USAF

Approved:

Lt Col Raymond C. Maple, PhD
(Chairman)

date

Dr. Peter J. Disimile (Member)

date

Dr. Mark F. Reeder (Member)

date

Abstract

This research modeled low-speed flow past idealized engine nacelle clutter in support of aircraft fire suppression research. The idealized clutter was comprised of three vertical rows of staggered circular cylinders approximating typical nacelle obstructions such as fuel lines and wire bundles. Single-phase, Detached-Eddy Simulations (DES) were conducted using the commercial CFD solver, *Fluent*TM, to resolve the flow-field dynamics inside the clutter element and determine mechanisms accounting for the failure of suppressant spray droplets from traversing the array under low-speed, free-stream conditions ($Re_D = 1,575$). The numerical models provided no evidence that span-wise vorticity or non-uniform shedding was responsible for transporting dispersed-phase particles towards the tunnel walls for deposition. However, the simulations demonstrated that suppressant droplets would likely follow a path governed by the vector sum of the local carrier fluid velocity and the velocity imposed by gravity. Additionally, the Stokes number was computed from time-accurate data to determine the ability of dispersed particles to negotiate the clutter element without impinging on a cylinder. For slower free-stream velocities, $U_\infty = 1 \text{ m/s}$, suppressant droplets ($D = 90 \text{ }\mu\text{m}$) will likely be entrained in vortices shed from the intermediate row of cylinders and subsequently deposited on the last row of cylinders as the Karman vortex directly collides with the clutter. At free-stream velocities, $U_\infty = 5 \text{ m/s}$, the droplet particles will likely fail to track the carrier fluid streamlines in the cylinder wake and remain free of any shed vortices. Thus, the suppressant will conceivably transit the cylinder array without impact. These findings imply that a bluff-body turbulent diffusion flame in a cylinder wake could be nearly impossible to extinguish under high-speed, co-flow conditions. Conversely, suppressant transported by low-speed co-flow would experience difficulty traversing the cylinder array and reaching a downstream fire.

Acknowledgements

I would like to thank my adviser, Lt Col Raymond Maple, for guiding my research efforts and for taking the time to teach me many of the subtleties of computational fluid dynamics. Also, I owe thanks to Dr. Peter Disimile and Dr. Mark Reeder for their assistance in this research. Thanks also to Aaron McClung who often loaned me his Linux expertise. And finally, my deepest gratitude goes to my wife who has supported me throughout the AFIT ordeal.

Matthew S. Caspers

Table of Contents

	Page
Abstract	iv
Acknowledgements	v
List of Figures	viii
List of Tables	x
Nomenclature	xi
Abbreviations	xii
I. Introduction	1
1.1 Engine Nacelle Fire Suppression	1
1.2 Research Objective	4
1.3 Research Approach	4
II. Background and Theory	6
2.1 Circular Cylinder in Cross-Flow	6
2.2 Turbulence	7
2.3 Turbulence Modeling	9
2.3.1 Detached-Eddy Simulation	14
2.3.2 Free-stream Turbulence Intensity for Spalart-Allmaras Based DES	16
2.3.3 DES Grids	17
2.3.4 DES Time Step	19
2.3.5 Grid Convergence	19
2.4 Droplet Transport	20
2.4.1 Inertial Analysis	20
2.4.2 Stokes Number	20
2.5 CFD Cylinder Research	21
III. Methodology	23
3.1 Clutter Geometry	23
3.2 Test Matrix	23
3.3 RANS Grid Generation	25
3.4 DES Grid Generation	26
3.4.1 Space/Time Coupling	27
3.5 Fluent Setup	29

	Page
3.5.1	RANS Specific Setup 31
3.5.2	Detached-Eddy Simulation Specific Setup 32
3.6	Visualization Tool Kit and Post-Processing 32
IV.	Results 37
4.1	Single Cylinder DES Validation 37
4.1.1	Boundary Layer Resolution 37
4.1.2	Spectral Content 37
4.2	Exploration of the Circular Cylinder Array 41
4.2.1	Boundary Layer Resolution 41
4.2.2	Spectral Content 42
4.3	Droplet Transport Mechanisms 46
4.3.1	Particle Transit Time Analysis 47
4.3.2	Stokes Number Analysis 52
V.	Conclusions 57
5.1	Detached-Eddy Simulation 57
5.2	Droplet Transport 57
5.3	Future Research 58
5.4	Summary 60
Appendix A.	Ancillary CFD Discussions 62
A.1	Modified Turbulent Viscosity and Turbulence Intensity 62
A.2	RANS to DES Transient Artifacts 64
Bibliography 66
Vita 69

List of Figures

Figure		Page
1.1.	Idealized Engine Nacelle Clutter Elements	3
1.2.	Clutter of Disimile et al.	3
2.1.	Karman Vortex Streets	6
2.2.	Turbulent Boundary Layer Vis.	8
2.3.	DES Grid Regions	17
3.1.	Idealized Engine Nacelle Clutter for CFD Model	24
3.2.	DES Grid	27
3.3.	RANS-LES Transition Location	28
3.4.	Sub-iteration Comparison	33
3.5.	VTK Bounding Box	34
4.1.	Single Cylinder Wall y^+	38
4.2.	Boundary Layer Profile, Single Cylinder	38
4.3.	Boundary Layer Measurement Location	39
4.4.	Strouhal Number Measurement Location	39
4.5.	PSD, Single Cylinder	40
4.6.	Cylinder Array Wall y^+	41
4.7.	Designation of Cylinders in the Array	42
4.8.	Boundary Layer Profiles, Cylinder Array, 9.9M Cells	43
4.9.	PSD, Cylinder Array, 9.9M Cells	44
4.10.	PSD, Cylinder Array, 14M Cells	45
4.11.	Vortex Core Time Evolution	47
4.12.	Sngl. Cyl. Vortex Core Time Evolution	48
4.13.	Y-Velocity Vis. 1 m/s , Single Cyl.	49
4.14.	Vorticity Vis. 1 m/s , 14M Cells	50
4.15.	Y-Velocity Vis. 1 m/s , 14M Cells	51

Figure		Page
4.16.	Stokes Number Vis. 1 m/s , 14M Cells	52
4.17.	Stokes Number Evolution, 1 m/s , 14M Cells	53
4.18.	Stokes Number Vis. 5 m/s , 14M Cells	54
4.19.	Stokes Number Evolution, 5 m/s , 14M Cells	55
A.1.	Modified Turbulent Viscosity Comparison	63
A.2.	Avg. x,z Velocity Vis. 5 m/s , 14M Cells	65

List of Tables

Table		Page
3.1.	Test Matrix	25

Nomenclature

<i>Symbol</i>	<i>Description</i>
C_{DES}	DES model constant
\tilde{d}	DES length scale
d_w	Distance to the wall
D	Cylinder Diameter
δ	Boundary Layer Height
Δ	Local grid cell spacing
Δ_0	Objective grid cell spacing
Δx	Local grid cell spacing in the x-direction
Δy	Local grid cell spacing in the y-direction
Δz	Local grid cell spacing in the z-direction
η	Kolmogorov length scale
f	Frequency (Hz)
λ	Wavelength
ν	Kinematic viscosity (m^2/s)
ν_t	Turbulent (eddy) viscosity (m^2/s)
$\tilde{\nu}$	Modified turbulent viscosity (m^2/s)
μ	Molecular Viscosity (kg/ms)
Re	Reynolds number
St	Strouhal number
Stk	Stokes number
U_∞	Free-stream velocity
y^+	Non-dimensional wall-normal (y) variable

Abbreviations

<i>Abbreviation</i>	<i>Description</i>
AENFTS	Aircraft Engine Nacelle Fire Test Simulator
CFD	Computational Fluid Dynamics
CFL	Courant-Friederichs-Lewy Number
DES	Detached-Eddy Simulation
DNS	Direct Numerical Simulation
FVE	Fluent VTK Extractor
LES	Large-Eddy Simulation
NGP	Department of Defense Next Generation Fire Suppression Technology Program
RANS	Reynolds Averaged Navier-Stokes
SGS	Subgrid Scale
TI	Turbulence Intensity
VTK	Visualization Toolkit

CFD INVESTIGATION OF FLOW PAST IDEALIZED ENGINE NACELLE CLUTTER

I. Introduction

1.1 *Engine Nacelle Fire Suppression*

The aircraft engine nacelle environment is particularly conducive to the outbreak of fire as a result of the myriad of ignition sources such as chaffed electrical wiring, hot surfaces, and the abundance of fuel from leaking or damaged jet fuel, oil, or hydraulic lines. Ambient air typically enters the engine nacelle through vents or actuated doors and is used to cool the engine core and avionics, as well as disperse flammable vapors which would otherwise linger near hot surfaces. In the event of a fire, the flow of cooling air through the nacelle has the undesirable effect of diluting a dispensed fire suppressant and raising the probability of re-ignition. As cooling air flows through the nacelle it is forced to navigate a labyrinth of clutter in the form of wire bundles, fuel lines, oil pumps, avionics boxes, and structural members such as ribs and stringers. The obstructions give rise to all types of flow irregularities in an already highly turbulent free-stream flow field. Given these conditions, the most likely type of nacelle fire is either a turbulent diffusion flame stabilized by a clutter element or a pool fire guarded by an obstruction. [1] Naturally, the ability to extinguish a nacelle fire is paramount to the safety and survivability of the aircraft and crew.

In use since the 1950s, Halon 1301 (CF_3Br) is operationally proven to be the fire suppressant of choice for both military and commercial aircraft engine nacelles. As a result of the Montreal Protocol on Substances that Deplete the Ozone Layer, the production of Halon was banned as of January 1, 1994 forcing the Department of Defense to rely on its stockpiles of Halon 1301 for aircraft fire suppression. [13] The ban sparked the creation of the U.S. Air Force Halon Replacement Program for Aviation and the Department of Defense Next Generation Fire Suppression Technol-

ogy Program (NGP); both programs were responsible for evaluating alternative extinguishants and developing technology demonstrations of environmentally-friendly, economical methods for fire suppression and halon replacement. The NGP primary areas of study included fire extinguishant chemistry and toxicity testing, developing new aerosol suppressants, improving methods of suppressant delivery, and the examination of new suppression mechanisms and technology. [17] Because Halon 1301 extinguishes aircraft fires so efficiently, research to characterize the flow field and optimize suppressant delivery had little pay-off until the production ban and the initiation of the NGP. [7]

At the outset of the NGP and the Air Force Halon Replacement Program for Aviation, extensive testing was conducted at the Aircraft Engine Nacelle Fire Test Simulator (AENFTS) facility located at Wright-Patterson Air Force Base in Dayton, Ohio. The AENFTS is constructed to represent the geometry and flow fields associated with aircraft engine nacelles. As part of the NGP, factors such as extinguishant temperature, pressure, and distribution, ventilation air pressure and velocity, clutter size and configuration, and fire location were examined at the AENFTS facility and correlated in an effort to develop metrics for evaluating fire suppression. The experimental characterization of nacelle fires provided insight into airflow velocities and initial estimates of minimum agent concentrations necessary for fire suppression. [1,13] However, the details of agent transport were still largely unexamined.

Working under the suppressant transport branch of the NGP, Disimile et al. [7] experimentally explored water droplet transport past idealized engine nacelle clutter. Idealized clutter models are simplified representations of actual engine nacelle clutter elements which approximate complicated nacelle obstructions allowing investigators to isolate geometric variables. For example, structural ribs are approximated as simple fences, wire bundles and fuel lines are simplified as either a single cylinder or an array of cylinders, and extremely dense areas of clutter are approximated as tightly packed spheres or porous media (Figure 1.1). [10]

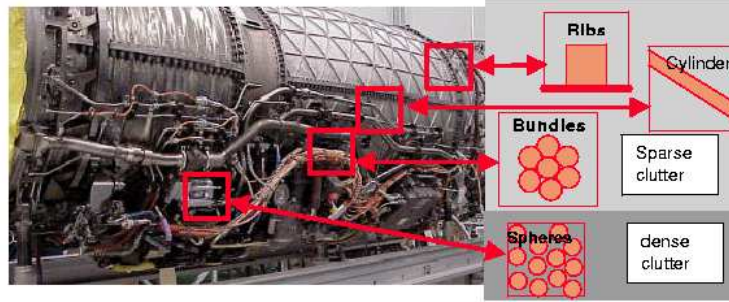


Figure 1.1: Idealized Engine Nacelle Clutter Elements [17]

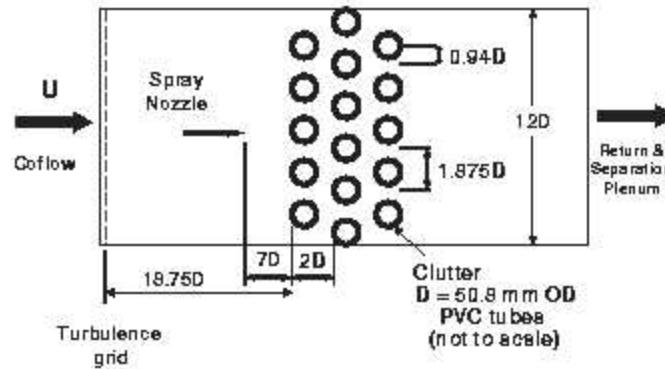


Figure 1.2: Idealized Engine Nacelle Clutter Element of Disimile et al. [7]

The generic clutter package of Disimile et al. shown in Figure 1.2 was comprised of circular cylinders each 50.8 mm in diameter arranged in an array of three equally spaced rows of five, six, and five cylinders. The study examined the effect of two variables, free-stream airspeed and cylinder spacing, on the amount of suppressant transported past the clutter package. The cylinder spacing was varied from $0.25D$ to $2.0D$, and the free-stream airspeed was examined over a range of 0.5 m/s to 6.5 m/s . Disimile et al. found that for large clutter spacing ($2.0D$) and higher airspeeds (5 m/s) upwards of 95% of the water spray was transported past the clutter package. However, for tight stream-wise cylinder spacing ($0.25D$) and lower airspeeds ($0.5\text{--}2 \text{ m/s}$) less than 40% of the suppressant was transported past the clutter. [7]

1.2 *Research Objective*

Because of the growing need to accurately understand flow field dynamics inside an engine nacelle for fire suppression applications, this research seeks to characterize the unsteady flow dynamics inside the idealized engine nacelle clutter of Disimile et al. and ascertain the mechanisms of droplet transport and entrapment observed by Disimile et al. Naturally, a deeper understanding of the processes contributing to transport and collection of entrained droplets inside engine nacelles is crucial to formulating a comprehensive nacelle fire suppression strategy.

1.3 *Research Approach*

Investigation of flow dynamics inside the idealized clutter element of Disimile et al. and the analysis of droplet transport phenomena was accomplished by performing numerical simulations of the flow-field using the commercial Computational Fluid Dynamics (CFD) solver, *Fluent*TM. Detached-Eddy Simulation (DES), a relatively recent addition to the turbulence modeling arsenal, was selected as the primary turbulence modeling technique because the turbulent structures most likely coupled to fire suppression and droplet transport are not adequately captured by mean flow quantities. Simulations to validate DES as an acceptable model in low Reynolds number flows were conducted first on a single cylinder grid. Subsequently, DES was applied to a scaled version of the idealized nacelle clutter developed by Disimile et al. at two distinct free-stream airspeeds. Unlike the experiment of Disimile et al., the numerical simulation did not include a dispersed-phase model for particle tracking. Instead, this research focused on resolving the flow-field dynamics and pinpointing aspects of the flow which might explain the droplet transport phenomena.

Two hypotheses explaining the transport and the entrapment of entrained suppressant droplet particles were specifically tested in this investigation. One hypothesis postulated that non-uniform, span-wise shedding was generating waves along the span and essentially pushing entrained water droplets towards the tunnel walls. After deposition on the tunnel walls, the droplets coalesce and drip to the tunnel floor forming

a pool of suppressant. Another hypothesis submits that droplet transport is governed primarily by the combination of inertial and fluid dynamic influences instead of flow-field dynamics alone. More specifically, the path of an entrained particle is determined by the relationship between the characteristic inertial and flow times of the dispersed-phase system. This relationship ultimately guides the particle along either a ballistic path or directs the particle along the flow's streamlines.

The following chapters discuss in detail the theory, methodology, and findings of the numerical simulations of flow past idealized clutter elements and relate the results to engine nacelle fire suppression.

II. Background and Theory

As stated in Section 1.1, nacelle fire suppression and the NGP cover a wide range of topics from suppressant chemistry and toxicity to delivery and operational concerns. This research, however, narrows the scope of interest primarily to nacelle flow-field dynamics and suppressant delivery. In this chapter, discussion is devoted to flow-field dynamics of a cylinder in cross-flow, turbulent flow characteristics, and turbulence modeling techniques such as Detached-Eddy Simulation (DES).

2.1 *Circular Cylinder in Cross-Flow*

As early as Leonardo da Vinci, who sketched the wakes of bluff bodies in the fifth century, scientists have studied the circular cylinder in cross-flow. The phenomenon of vortex shedding from a bluff body is widely known and has born significant scrutiny over a wide range of free-stream conditions. [5, 11, 18, 19, 28] The potential solution for flow past a circular cylinder predicts symmetrical streamlines about the cylinder and computes the flow at the surface of the cylinder in polar coordinates as $u_r = 0$ and $u_\theta = -2U_\infty \sin \theta$. In reality, the potential solution violates the no-slip condition at the wall and is completely non-physical. Visualization of flow past a cylinder reveals distinct alternating vortices shed from the top and bottom of the cylinder called Karman vortex streets. In 1911, von Karman showed that the vortex street (Figure 2.1), clearly evident for Reynolds numbers of $40 < Re_D < 150$, is a stable energy configuration of the flow. [18] As the Reynolds number increases ($Re_D > 10^5$), vortex shedding remains a defining feature, but the vortex streets decay quickly downstream of the cylinder due to turbulent dissipation. In 1878, Strouhal quantified the periodic shedding frequency associated with bluff bodies and related it to free-stream velocity and body diameter.

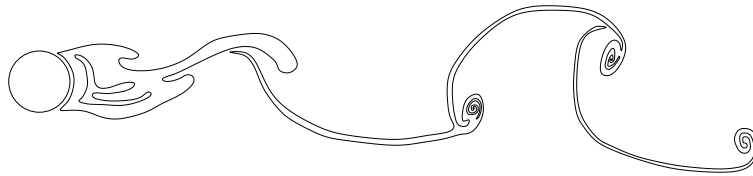


Figure 2.1: Depiction of Karman vortex streets, $Re \approx 160$

The Strouhal number, a non-dimensional parameter, is given by

$$St = \frac{fD}{U} \quad (2.1)$$

where f is the frequency of the vortex shedding, D is the cylinder diameter, and U is the free-stream velocity. The accepted Strouhal number for Reynolds numbers of $100 < Re < 10^5$, correlated by Rayleigh in 1879, is approximately 0.2. [18, 28]

2.2 *Turbulence*

Turbulence, often characterized by high Reynolds numbers, is a flow regime distinguished by the generation, transport, and destruction of three-dimensional vortex structures. Smoke issuing from a smokestack is a common example of the production, convection, and dissipation of turbulence. [24].

As turbulent eddies move through the flow, large amounts of mass, momentum, and energy are redistributed. Unlike laminar flow where the method of momentum transfer is molecular diffusion, the dominant mode of momentum transfer is the large, mixing vortices. From an engineering standpoint, turbulence serves to improve the mixing of fuel and oxidizer in combustion reactions and plays a role in controlling flow separation. Energy and momentum transferred from the mean flow into a turbulent boundary layer serves to excite the flow and stave off separation when compared to laminar flow. The dimples on a golf ball force the boundary layer to become turbulent in order to take advantage of increased turbulent mixing and prolonged separation. [3, 24]

Another defining characteristic of turbulence is fluid motion over an expansive range of length and time scales. An observer watching smoke emanating from a stack would note that the largest eddies are on the order of the diameter of the stack. Likewise in a turbulent boundary layer, the scale of the largest turbulent structures are on the order of the boundary layer thickness, δ , and are associated with the integral length scale. Eddies at the integral scale are very energetic and usually the direct

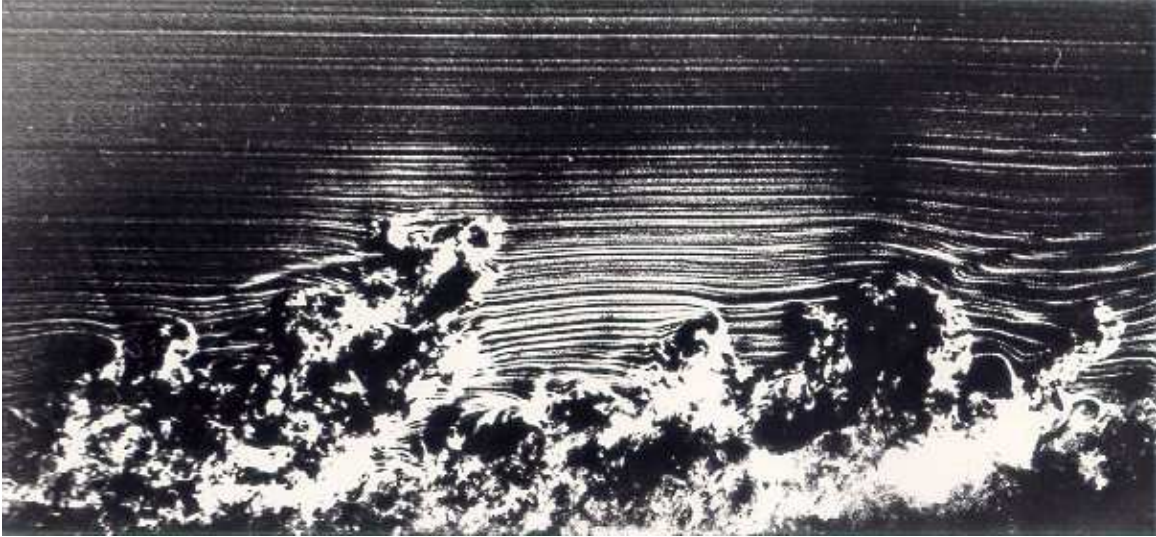


Figure 2.2: Turbulent boundary layer visualization at $Re = 3500$ illustrating the range of length scales inherent in turbulent flow [8]

result of a flow's turbulence generation mechanism. [3] With respect to a cylinder in cross-flow, the integral scale is on the order of the diameter of the cylinder and is observed directly in a Karman vortex.

Returning to the smokestack example, an observer would notice over time large vortex structures breaking down and giving way to smaller vortices. Each time smaller vortices are born from a larger vortex, kinetic energy is transferred to a smaller scale in the flow. The cascade of energy across the spectrum of length and time scales is a fundamental aspect of turbulence. The energy continuously cascades from the integral scale down to the smallest scale, the Kolmogorov scale, η , where turbulent kinetic energy is dissipated directly to heat via molecular viscosity. [24] Accurately accounting for the energy cascade is crucial to modeling turbulence and computing its effects. Relative to the large, integral scale eddies of the flow, the smallest eddies occur on a very short time scale. Kolmogorov postulated that the rate at which the smallest eddies received energy from the largest eddies was approximately equal to the rate of dissipation to heat. This relationship is known as Kolmogorov's universal equilibrium theory. [29] Computation of the Kolmogorov length scale based on the

universal equilibrium theory supports the concept that turbulence is a continuum phenomenon since η is much greater than the mean free path of a molecule, λ .

In summary, turbulent flow is a seemingly random and inherently three-dimensional fluid motion characterized by unsteadiness and mixing eddies over a vast range of length and time scales. The eddies and fluctuations associated with the dynamics of turbulence in contrast with laminar flow force definite interactions between the layers of the fluid which leads to increased momentum and energy transfer.

2.3 Turbulence Modeling

Computational Fluid Dynamics (CFD), in general, refers to numerically solving the discretized Navier-Stokes equations which govern the motion of fluid in a continuum. When the flow physics require accounting for turbulence in a numerical solution, additional computational expenses are introduced. Although the motion of turbulence may seem random, the fluid motion is still governed by the Navier-Stokes equations. Thus, one method of computing a turbulent flow solution is Direct Numerical Simulation (DNS), which solves the Navier-Stokes equations directly and resolves the entire spectrum of turbulent length and time scales, thus capturing the energy cascade discussed in Section 2.2. However, the drawback to such an approach is that the required number of grid points scales with $Re^{9/4}$ which leads to a CPU time proportional to Re^3 and restricts DNS to problems with Reynolds numbers on the order of $10^4 - 10^5$ based on the largest current supercomputing capabilities. The complexity of turbulence usually forces the adoption of turbulence models to approximate the elements of turbulence to solve engineering problems in a timely, affordable manner. [4]

For many engineering applications, mean flow dynamics are the primary focus not the individual fluctuations caused by the turbulent eddies. When this is the case, the Reynolds Averaged Navier Stokes (RANS) equations can be used to compute mean flow quantities by time averaging the Navier-Stokes equations. This is accomplished

by substituting an average and fluctuating component into the equations for each of the variables. For instance, velocity becomes

$$u_i = \bar{u}_i + u'_i \quad (2.2)$$

After substituting the mean plus fluctuation terms, the equations are averaged. Either time or spatial averaging may be applied. However, time averaging is appropriate to statistically stationary turbulence while spatial averaging is more appropriate for homogeneous turbulence. Since the average of a fluctuation is zero, all averaged terms containing a fluctuation are eliminated except for the terms containing the average of the product of two fluctuations; these terms are most certainly non-zero. The resulting RANS equations are as follows [4]

$$Mass : \frac{\partial \bar{\rho}}{\partial t} + \frac{\partial}{\partial x_i} (\bar{\rho} u_i + \rho u'_i) = 0 \quad (2.3)$$

$$Momentum : \frac{\partial \bar{\rho} \bar{u}_i}{\partial t} + \frac{\partial}{\partial x_j} (\bar{\rho} \bar{u}_i \bar{u}_j) = -\frac{\partial \bar{P}}{\partial x_i} + \frac{\partial}{\partial x_j} (\bar{\tau}_{ij} - \overline{\rho u'_i u'_j}) \quad (2.4)$$

where

$$\begin{aligned} \bar{\tau}_{ij} &= 2\mu \bar{S}_{ij} - \frac{2}{3}\mu \frac{\partial \bar{u}_k}{\partial x_k} \delta_{ij} \\ \bar{S}_{ij} &= \frac{1}{2} \left(\frac{\partial \bar{u}_i}{\partial x_j} + \frac{\partial \bar{u}_j}{\partial x_i} \right) \end{aligned} \quad (2.5)$$

The energy equation is similarly derived using fluctuations and time averaging. While RANS methods exclude the need to calculate the fluctuations of each flow quantity, RANS does however introduce a new term: The Reynolds Stress Tensor, $-\overline{\rho u'_i u'_j}$. The Reynolds Stress is related to the momentum transfer that arises from the turbulent fluctuations and introduces a closure problem to the RANS equations. There are two methods for computing the Reynolds Stresses: first and second order closures. Second order closures are obtained by deriving exact equations for the Reynolds stresses by computing a second moment. This introduces additional, higher-order, unknown cor-

relations. Application of empirical data is necessary to determine the new unknowns. First order closures, on the other hand, employ the eddy viscosity hypothesis and calculate a turbulent viscosity for the flow. [4]

The Boussinesq eddy viscosity hypothesis approximates the Reynolds Stresses and provides closure to the RANS equations by assuming that the turbulent shear stress is related to the mean strain rate by a proportionality factor known as the eddy viscosity, μ_T .

$$\bar{\tau}_{ij}^T = -\overline{\rho u_i u_j} = 2\mu_T \bar{S}_{ij} - \frac{2}{3}\mu_T \frac{\partial \bar{u}_k}{\partial x_k} \delta_{ij} \quad (2.6)$$

As a result, the laminar flow Navier-Stokes equations are mathematically identical to RANS formulation. The only difference is that the viscosity, μ , is replaced with the sum of the molecular and eddy (turbulent) viscosities. In this research, only incompressible flows are of concern, therefore the terms associated with the divergence of velocity, $\frac{\partial \bar{u}_k}{\partial x_k}$, are neglected in both Equations (2.5) and (2.6).

$$\mu = \mu_L + \mu_T \quad (2.7)$$

The molecular (laminar) viscosity may be computed using Sutherland's Law since it is a property of the fluid. While the eddy viscosity assumption eliminates the need to compute the Reynolds Stress Tensor directly, it does not eliminate the requirement to compute a reasonable estimate of the turbulent viscosity.

Calculation of the eddy viscosity is accomplished using either a zero-, one-, or two-equation model. Zero-equation or algebraic models are so named because they do not involve solving a differential equation model and instead compute the eddy viscosity based on an algebraic formulation related to the velocity profile. A one-equation model, adds complexity by solving a single differential equation to govern the transport, generation, and destruction of turbulence. The most elaborate RANS models employ two differential equations to govern turbulent kinetic energy and turbulence

dissipation. Because this research employs the Spalart-Allmaras turbulence model, attention will now be focused on the development and theory of the Spalart-Allmaras one-equation turbulence model.

P.R. Spalart and S.R. Allmaras developed a model for the transport of a modified eddy viscosity, $\tilde{\nu}$, based on Galilean invariance, dimensional analysis, and empirical data. Galilean invariance is the concept that fundamental laws of physics are the same for all reference frames. Spalart and Allmaras developed their equation for eddy viscosity term by term, adding constants and functions to calibrate the model, against empirical data from free shear flows, wakes, and boundary layers. Since Spalart and Allmaras were developing a one-equation model focusing on application to aerodynamic flows, they elected to abandon the classical approach of tweaking their model for homogeneous turbulence and proceeded directly to a transport-diffusion model and calibrated the model at that level. The resulting Spalart-Allmaras turbulence model is as follows: [22]

$$\frac{\partial \tilde{\nu}}{\partial t} + u_i \frac{\partial \tilde{\nu}}{\partial x_i} = c_{b1} \tilde{S} \tilde{\nu} + \frac{1}{\sigma} [\nabla \cdot ((\nu + \tilde{\nu}) \nabla \tilde{\nu}) + c_{b2} (\nabla \tilde{\nu})^2] - c_{w1} f_w \left(\frac{\tilde{\nu}}{d_w} \right)^2 \quad (2.8)$$

$$\begin{aligned} \nu_t &= f_{v1} \tilde{\nu} \\ \tilde{S} &= f_{v3} S + \frac{\tilde{\nu}}{\kappa^2 d_w^2} f_{v2} \\ S &= \left| \frac{\partial u_i}{\partial x_j} - \frac{\partial u_j}{\partial x_i} \right| \\ \chi &= \frac{\tilde{\nu}}{\nu} \\ f_{v1} &= \frac{\chi^3}{\chi^3 + c_{v1}^3} \\ f_{v2} &= \left(1 + \frac{\chi}{c_{v2}} \right)^{-3} \\ f_{v3} &= \frac{(1 + \chi f_{v1})(1 - f_{v2})}{\max(\chi, 0.001)} \end{aligned}$$

$$\begin{aligned}
f_w &= \left(\frac{1 + c_{w3}^6}{g^6 + c_{w3}^6} \right)^{1/6} \\
g &= r + c_{w2} (r^6 - r) \\
r &= \frac{\tilde{\nu}}{\tilde{S} \kappa^2 d_w^2} \\
c_{b1} = 0.1355, \sigma &= 2/3, c_{b2} = 0.622, \kappa = 0.41 \\
c_{v1} &= 7.1, c_{v2} = 5 \\
c_{w1} &= \frac{c_{b1}}{\kappa^2} + \frac{(1 + c_{b2})}{\sigma} = 7.1 \\
c_{w2} &= 0.3, c_{w3} = 2
\end{aligned}$$

The first term on the left hand side of Equation (2.8) represents the time rate of change of the modified turbulent viscosity, $\tilde{\nu}$, and the second is the convective term. Generation of $\tilde{\nu}$ is represented by the first term on the right hand side and is followed by the turbulent and viscous diffusion terms. The final term on the right hand side controls the destruction of modified turbulent viscosity. Also, the above version of the Spalart-Allmaras turbulence model does not include the trip terms suggested by Spalart to allow the user to designate transition from laminar to turbulent flow, because the option is not provided in *Fluent*TM. [9]

To conclude the discussion of eddy viscosity, one should note that although the turbulent viscosity has the same units as the molecular viscosity, it is not a fluid property, but is instead representative of the flow and is problem dependent.

As discussed in Section 2.2, turbulence is characterized by a eddies over a wide range of time and length scales. The bulk of the momentum transfer throughout the flow is done by the largest eddies, which are more problem dependent. From the Kolmogorov universal equilibrium theory, the smaller eddies are generally more uniform and easier to model from one problem to the next. Directly computing the large eddies by using filtered equations and modeling only the smallest eddies is called Large Eddy Simulation (LES). The governing equations for Large Eddy Simulation (LES)

are obtained by filtering the Navier-Stokes equations with a filtering function based on either wave number or physical space. [4,9] The resulting filtered equations govern only the dynamics of the eddies larger than the filter width. *Fluent's*TM method of filtering the governing equations is implicitly accomplished by using the cell volume as the filtering function. Even though the smallest eddies are filtered from the governing equations, the energy cascade to the smallest eddies cannot be neglected. Subgrid Scale (SGS) models account for the energy cascade associated with eddies smaller than the filter width by modeling the dissipation of turbulent kinetic energy to heat. *Fluent's*TM LES SGS models apply the BoussinesqDES is able to switch seamlessly between LES and RANS formulations because a single velocity field is computed thereby eliminating discontinuities at the RANS and LES transition. hypothesis used in RANS computations and most use a basic mixing length model to compute the eddy viscosity. [9] Although LES allows for coarser grids and larger time steps than those required by DNS, the number of grid points, N , for an LES of a turbulent boundary layer still scales with Re^2 . [14] In particular, LES requires large numbers of cells in the boundary layer making it impractical for many engineering applications.

2.3.1 Detached-Eddy Simulation. In an effort to reduce the computational requirements of computing turbulent flow while still maintaining the time-accurate large eddies that LES resolves, Spalart formulated a method known as a Detached-Eddy Simulation (DES). DES is a three-dimensional, unsteady turbulence modeling technique which makes use of both LES and RANS methods. DES models switch from LES mode to RANS mode implicitly based on the grid density and the distance to the closest wall. When the model is operating as an LES, it is capable of resolving eddies on the order of the cell spacing, Δ . [2,25] The model carries the designation Detached-Eddy because it only resolves large eddies which are detached, or at a distance from a wall, as determined by the grid cell size. [25]

In *Fluent*TM, the DES model uses a Spalart-Allmaras turbulence model for its RANS mode. While DES is not strictly tied to the Spalart-Allmaras model, it does

offer a convenient length scale to use as the DES parameter. [25] In order to transform the ordinary RANS Spalart-Allmaras turbulence model into a DES, a slight modification to the equation is required. The distance to the wall, d_w , in the original Spalart-Allmaras transport equation is replaced by a quantity, \tilde{d} , which is the lesser of two quantities: the grid spacing, Δ , or the distance to the wall, d_w . [23]

$$\begin{aligned}\tilde{d} &= \min(C_{DES}\Delta, d_w) \\ \Delta &= \max(\Delta x, \Delta y, \Delta z)\end{aligned}\tag{2.9}$$

The constant, C_{DES} , is typically set to 0.65 based on calibration in isotropic turbulence.

With this modification to the Spalart-Allmaras length scale, the model switches automatically from a RANS formulation near the wall to an LES/SGS away from the wall. When using a pure RANS model throughout the domain, the eddy viscosity is designed to drop off to zero in the free-stream where no turbulence is modeled. By altering the length scale of the Spalart-Allmaras turbulence model, the turbulent production and destruction terms in Equation (2.8) cannot become zero in the free-stream thereby allowing the generation, transport, and dissipation of eddy viscosity on the subgrid scale. In the LES region, turbulent structures smaller than the grid cell size are modeled by the Spalart-Allmaras turbulence model functioning as an SGS eddy viscosity model while larger eddies in the flow are directly resolved. DES is able to switch seamlessly between LES and RANS formulations because a single velocity field is computed thereby eliminating discontinuities at the RANS and LES transition.

The behavior of the model is controlled by the user through grid design by controlling Δ . For example, the user should build a grid where $\Delta \gg \delta \geq d_w$ to trigger RANS behavior. [25] Conversely, in regions where an LES response is desired, the grid density should correspond to $\tilde{d} = C_{DES}\Delta$.

Grid refinement of a DES grid is often challenging because Δ , the local grid spacing, is the largest value of the spacing in the x, y, and z directions. Consequently, refinement in only one or two directions would be wasted; isotropic grid density is the goal in the LES region. On the other hand, the severe anisotropy (high aspect ratio) of boundary layer grids is the mechanism for triggering a RANS response near a wall.

Once more, the only parameter that varies to alter the LES/RANS state is \tilde{d} . In engineering situations where resolution of the boundary layer eddies is not critical, DES offers a method for directly computing the large, turbulent flow structures dominating massively separated flows at an affordable computational cost.

2.3.2 *Free-stream Turbulence Intensity for Spalart-Allmaras Based DES.*

The turbulence intensity of a flow, which is defined as

$$I = \frac{u'}{u_{avg}} \quad (2.10)$$

where u' is the RMS of the velocity fluctuations and u_{avg} is the mean velocity, can significantly impact separation behavior. However, when using a DES model based on the Spalart-Allmaras turbulence model, specification of free-stream turbulence intensity has little impact on the outcome of the solution. In the absence of large scale eddies for direct evaluation, the Spalart-Allmaras SGS model estimates the effect of turbulence exclusively with $\tilde{\nu}$, the modified turbulent viscosity. As a result, setting a free-stream turbulence intensity at the inlet only serves to alter the value of the modified turbulent viscosity at the boundary. Furthermore, the Spalart-Allmaras turbulence model is insensitive to high values of $\tilde{\nu}$ in the free-stream and damps disturbances quickly in the absence of turbulence generation. In the current effort, free-stream turbulence intensity would be an interesting variable to examine, but the limitations of the Spalart-Allmaras SGS model prevent a meaningful analysis of free-stream turbulence intensity when using DES. [4, 22]

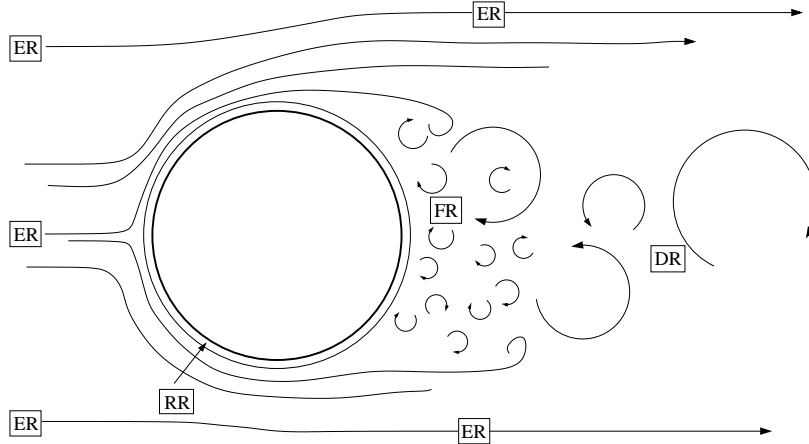


Figure 2.3: DES Grid Regions; ER = Euler Region, RR = RANS Region, FR = Focus Region, DR = Departure Region

2.3.3 DES Grids. Since DES combines RANS and LES methods into a single model, the complications associated with generating RANS and LES grids individually are also present in a DES grid generation. As discussed in Section 2.3.1, grid density controls the path a DES travels: RANS or LES. Before designing a DES grid, a user should be intimately familiar with the expected flow-field in each region of the grid.

A DES grid is divided into three Super-Regions: the Euler (ER), RANS (RR), and LES (LR) regions. The Euler Region of a DES mesh is typically located upstream of any turbulence generation and has cell spacing dictated only by geometry and shocks. Generally, coarse, isotropic cell spacing in all three directions prevails. [21] The RANS Region of the grid contains the flow's boundary layer and is itself comprised of the RANS Viscous and Outer Regions. The RANS Viscous Region under DES is identical to the near wall region of a purely RANS grid and is responsible for capturing the viscous sublayer, buffer layer and the log layer. When using the Spalart-Allmaras turbulence model in the RANS Region, Spalart recommends the spacing of the first cell in the wall-normal direction be at least $\Delta y^+ = 2$ or less. [21] *Fluent*TM suggests targeting a Δy^+ of one for the Spalart-Allmaras model. [9] Additionally, the wall-normal growth rate should be on the order of 1.25 or less to accurately capture the log layer.

In the wall-parallel direction, grid spacing is dictated by standard RANS methods and therefore shocks and geometry drive the requirements for the Δx^+ grid refinement. [21] In the RANS Outer Region, standard RANS grid spacing practices prevail. The cause for concern in this region is the free-stream/boundary layer interface. In the free-stream, eddy viscosity is near zero and may rapidly approach zero at the edge of the RANS region. For an accurate model, the boundary layer solution must detect a slope discontinuity in the eddy viscosity across the free-stream/boundary layer interface. As a result, a mesh's RANS Region is often extended well past the boundary layer height, δ . The solution is far more forgiving when δ is overestimated rather than underestimated. [21]

The LES Region is subdivided into two regions: the Focus (FR) and Departure (DR) Regions. As the name implies, the Focus Region is the area of the model where accurate resolution of the detached-eddies is desired. The objective cell spacing, Δ_0 , in the Focus Region quantifies the spatial resolution of a DES. Grid spacing in the FR should be isotropic since $\Delta = \max(\Delta x, \Delta y, \Delta z)$ defines the local grid density and serves to filter out turbulent eddies on the order of the local grid cell size. Once more, the user should remember that refining the FR mesh in only one or two directions wastes computational resources (Section 2.3.1). Finally, the Departure Region is found adjacent to the FR and transitions the LES grid spacing of Δ_0 to coarser cell spacing often on the order of Euler spacing near grid boundaries. Essentially, the DR serves as a good numerical neighbor to the Focus Region and only imposes a moderate computational cost on the solver. Results in this region of the mesh should not be accepted as spatially accurate since the motion of the resolved eddies is increasingly dominated by eddy viscosity as the grid density coarsens. Spalart suggests the following rule of thumb for determining how large to make the Focus Region and where to start the Departure Region. "Can a particle return from this [DR] point to very near the body? Is there flow reversal?" [21] If the answer to these questions is yes, then regions containing such phenomena should be included in the FR.

2.3.4 DES Time Step. Selection of a suitable time step for a Detached-Eddy Simulation (DES) is based on the the grid density of the Focus Region because the FR possesses the finest spatial resolution where unsteady turbulent structures are resolved. None of the other regions will likely present frequency content higher than the FR. Assuming that the SGS model is well calibrated, then the smallest, potentially active eddies would have a wavelength $\lambda \approx 5\Delta$. [21] Although these eddies are resolved, they are not particularly spatially accurate because their motion is governed by eddy viscosity and the cascade of energy to smaller eddies is modeled instead of directly computed. Given these conditions, Spalart recommends five time steps per period for a local Courant Number (CFL) of 1. This means that a wave (eddy) travels across one cell for every timestep. Thus, five samples per period will give a rudimentary sampling of the eddy. Based on these assumptions, a good starting point for selecting the solver time step, Δt is to apply the formula

$$\Delta t = \frac{\Delta_0}{U_{max}} \quad (2.11)$$

where Δ_0 is the targeted FR cell spacing and U_{max} is the maximum estimated velocity encountered in the FR. Spalart reminds the user that this formulation is only a starting point, and space/time balancing is encouraged since not all differencing schemes behave alike. [21]

2.3.5 Grid Convergence. Ideally for a DES solution, simulations are conducted at cell spacings of Δ_0 and $\Delta_0/2$. Of course, for some grids, halving the grid spacing in the FR can present an impossible computational burden so at the very least, the number of grid cells between the nominal grid and the convergence test grid should increase by a factor of the $\sqrt{2}$. [21] Due to the implicit relationship between space and time for a LES, both the grid spacing and the time steps size must be refined in order to conduct a complete grid convergence study.

2.4 Droplet Transport

2.4.1 Inertial Analysis. A simple, first-order estimate of dispersed-phase particle motion assumes that a droplet's path is governed exclusively by inertia and the local velocity vector of a carrier fluid. For this analysis, the vertical component of droplet drag is negligible, and an entrained droplet is assumed to move at a speed equal to the magnitude of the local velocity of the carrier fluid. However, the entrained droplet does not necessarily track the carrier fluid's streamlines exactly. Instead, the droplet traverses a path described by the vector sum of the carrier velocity and the velocity imposed by gravity. When this is the case, a droplet entrained in a fast moving carrier fluid could pass through the clutter array before gravity causes the particle to fall into one of the cylinders. Conversely, in slower flow-fields, the time required to pass the array may be significantly longer or on the order of the time required to fall into one of the clutter elements.

2.4.2 Stokes Number. Further analysis of droplet velocity and inertia involves computing the Stokes number throughout the flow-field. The Stokes number is defined as the ratio of the response time of a dispersed particle to the response time of the system. Essentially, the Stokes number is a non-dimensional parameter for characterizing the ability of entrained particles to negotiate obstacles. The Stokes number is given by

$$Stk = \frac{\tau_d}{t_s} \quad (2.12)$$

where the characteristic time of the droplet, τ_d , is given by

$$\tau_d = \frac{\rho_d d_d^2}{18\mu_c} \quad (2.13)$$

and ρ_d is the density of the droplet, d_d is the diameter of the droplet, and μ_c is the viscosity of the carrier fluid. Finally t_s , the system response time, is computed based on a characteristic length, L_s , and a characteristic velocity, V_s . With respect to the cylinder array, the characteristic length is the cylinder diameter because it poses the

most conservative estimate for the response time of the system. For Stokes numbers $Stk < 1.0$, the dispersed phase particles follow the streamlines of the carrier fluid closely. On the other hand, for $Stk > 1.0$ the path of the particles is increasingly governed by inertia and not the carrier fluid's streamlines. The smaller the Stokes number, the better a droplet will be able to negotiate an obstacle. [9]

2.5 CFD Cylinder Research

A single circular cylinder in cross-flow has been studied by a multitude of CFD RANS models. [2, 25, 26, 28, 29] However, with the advent of DES, many investigators have chosen to exercise DES on the circular cylinder problem and validate it as a viable option for computing bluff body flows. Travin et al. modeled laminar and turbulent separated flow past a circular cylinder using DES and found good agreement between the model and experimental data for drag, shedding frequency, pressure, and skin friction. [25] In another study, Vatsa et al. compared low speed flow past a circular cylinder with Reynolds number ranging from 5×10^4 to 1.4×10^5 using NASA Langley's production TLNS3D code for 2-D and 3-D URANS and DES models. Vatsa's group found that 3-D DES matched well with the experimental data and work of Travin et al. and judged 3-D DES an acceptable method for predicting highly separated flows. [26]

Unlike the single circular cylinder in cross-flow, an array of cylinders has borne little scrutiny by experimentalists and CFD practitioners alike. Most existing research in the realm of flow past an array of cylinders was accomplished for the purpose of determining and predicting heat transfer and vibration in heat exchanger tube bundles. Using a 2-D RANS method, Watterson et al. modeled the flow around a staggered array of cylinders in turbulent, low-speed cross flow ($Re_D = 21,000$). The numerical scheme of Watterson et al. [27] solved the governing Navier-Stokes equations via a pressure correction method and applied the low-Reynolds number $k-\epsilon$ turbulence model of Yang and Shih. Wind tunnel results were compared to the numerical predictions of Watterson's group and achieved only marginal agreement

with experimental trends. [27] Seeking a higher fidelity model, Hassan and Barsamian explored the staggered tube bundle problem but instead employed a LES technique allowing spatial and temporal resolution of the large-scale turbulent eddies associated with the tube wakes at $Re_D = 21,700$. The LES results correlated very well with the same experimental data used by Watterson et al., and captured the high transverse turbulence intensities and the generation of span-wise vorticity aspects invisible to a 2-D RANS solution. [12]

III. Methodology

Obtaining a numerical solution for characterizing the flow-field dynamics inside an array of cylinders was an iterative and nearly simultaneous undertaking. The methodology of grid generation, numerical simulation, and data reduction were far from serial processes because each aspect was implicitly driven by the others. This chapter discusses each process in the solution and considers the links between each step.

3.1 Clutter Geometry

The clutter geometry for this research is patterned after the array of circular cylinders used by Disimile et al. [7] The principal difference between the two clutter packages is scale. The full-size wind tunnel setup used by Disimile incorporated cylinders with diameters $D = 50.8 \text{ mm}$ (2 in.) in a tunnel with a $610 \times 914 \text{ mm}$ ($24 \times 36 \text{ in.}$) cross-section. The clutter package for this research, however, was scaled down by a factor of two producing cylinder diameters of $D = 25.4 \text{ mm}$ (1 in.) and a tunnel cross-section of $304.8 \times 304.8 \text{ mm}$ ($12 \times 12 \text{ in.}$). This was done in order to match the experimental setup of an ongoing parallel research effort. Figure 3.1 represents the clutter geometry used in this research.

3.2 Test Matrix

Due to the significant computational time required to perform Detached-Eddy Simulation (DES), the scope of the investigation was narrowed to ensure data collection was completed in a timely manner. The work of Disimile et al. [7] indicated that low-speed ($0.5\text{--}2 \text{ m/s}$) flow coupled with tight stream-wise cylinder spacing ($0.25D$) posed a significant obstacle to water droplet transport past an array of circular cylinders acting as nacelle clutter. For this research, the cylinder spacing was fixed at $2.0D$.

The flow dynamics for an array of circular cylinders is not correlated to Reynolds number like it is for a single cylinder. However, matching the Reynolds number

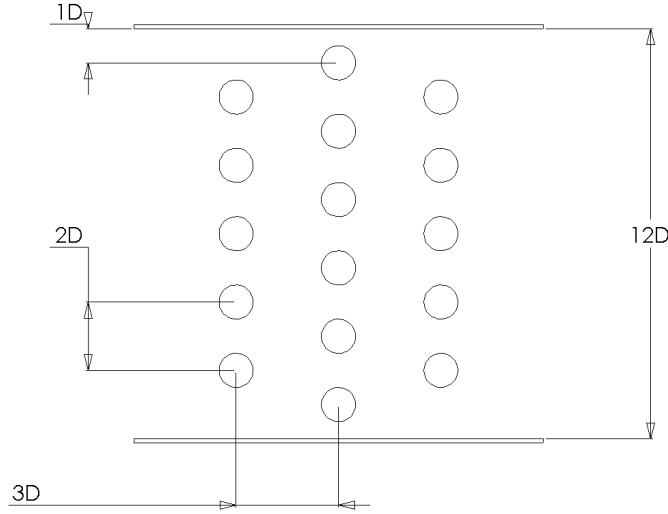


Figure 3.1: Idealized Engine Nacelle Clutter for CFD Model

of Disimile’s experiment to the CFD model was considered good practice. In this context, the Reynolds number of the cylinder array was defined as

$$Re = \frac{UD}{\nu} \quad (3.1)$$

where U is the free-stream velocity, D is the diameter of a cylinder, and ν is the kinematic viscosity. Because this research seeks to characterize mechanisms hindering the dispersement and transport of fire suppressant droplets, the low-speed realm of Disimile’s research was targeted. To maintain Reynolds number consistency between the experiment of Disimile et al. and the numerical model, a velocity of 1 m/s was used for the lower bound to match the 0.5 m/s of Disimile et al. The 5 m/s case, corresponding to Disimile’s 2.5 m/s case based on Reynolds number scaling provides another test point to explore and replicate the trends observed by Disimile et al. without reaching the upper bound of suppressant transport noted by Disimile.

Table 3.1 compiles the six test cases examined in this research used to search for mechanisms of droplet transport inside the clutter array. Instead of examining the test matrix one case at a time, the investigation progressed as a simultaneous

Table 3.1: Test Matrix of Numerical Simulations

Single Cylinder	Cylinder Array (9.9M Cells)	Cylinder Array (14M Cells)
$\Delta_0 = 0.2$	$\Delta_0 = 0.2$	$\Delta_0 = 0.1$
$U_\infty = 1 \text{ m/s}$ $\Delta t = 0.01 \text{ s}$	$U_\infty = 1 \text{ m/s}$ $\Delta t = 0.01 \text{ s}$	$U_\infty = 1 \text{ m/s}$ $\Delta t = 0.01 \text{ s}$
$U_\infty = 5 \text{ m/s}$ $\Delta t = 0.005 \text{ s}$	$U_\infty = 5 \text{ m/s}$ $\Delta t = 0.005 \text{ s}$	$U_\infty = 5 \text{ m/s}$ $\Delta t = 0.005 \text{ s}$

and iterative process. To start, 2-D single cylinder and the cylinder array grids were generated for computing RANS solutions to test initial estimates of boundary layer near-wall spacing. Between each simulation, the grids were tweaked until the wall y^+ proved satisfactory and the boundary layer profile was adequately captured. Next, the 2-D grids were extended into three dimensions, and RANS computations were again performed to verify wall y^+ and the boundary layer profile and height. With satisfactory RANS results in hand, Detached-Eddy Simulations were performed on the single cylinder grid to validate the DES model. Upon achieving satisfactory DES results for a single cylinder, Detached-Eddy Simulations were accomplished on the cylinder array grids. The following sections provide deeper insight into grid generation and the solution process. The grid spacing and dimensions discussed are the final values after iterating through several versions of each grid.

3.3 RANS Grid Generation

Grid generation was accomplished using the commercial software, *Gridgen*TM to generate 2-D and 3-D unstructured grids for DES. Developing node connectivity for an array of cylinders with $2.0D$ stream-wise spacing was the first task. After laying out the cylinder and tunnel wall locations, each cylinder was wrapped with a structured block containing hexahedral (quadrilateral in 2-D) cells which employed RANS spacing methods. Planning for the Spalart-Allmaras turbulence model, initial wall-normal spacing was set at 7.25×10^{-4} for the hyperbolically-generated, structured boundary layer which grew at a rate of 1.125 for fifteen cells and then switched to a growth rate of 1.5 until the cells reached approximately unit aspect ratio. For

an exclusively RANS computation, the span-wise spacing was not critical and was therefore set equal to the nominal size of the tetrahedral (triangular in 2-D) cells comprising the majority of the domain. Generation of the unstructured, tetrahedral (triangular in 2-D) cells was accomplished using Delaunay triangulation in *Gridgen*TM. In order to save on computational time, the boundary layers on the tunnel walls were not modeled. The coarser wall-normal grid density associated with inviscid walls still captured pressure gradients and reflections from the wall, but significantly reduced data storage and computational requirements.

3.4 *DES Grid Generation*

The RANS grid described in Section 3.3 eventually evolved into a DES grid after considering factors pertinent only to DES. Since the user indirectly controls when the solver switches from RANS to LES, properly estimating the boundary layer is crucial to determining appropriate grid spacing. Prandtl’s formulation for the thickness of a turbulent boundary layer on a flat plate was applied.

$$\delta_{99} = \frac{0.37x}{\sqrt[5]{Re_x}} \quad (3.2)$$

where x is a characteristic length and Re_x is the Reynolds number based on x . This estimation gives $\delta_{99} = 0.06$ in. The quarter-circumference of the cylinder was designated as the characteristic length because the critical boundary layer height occurs at a location near the top and bottom of the cylinder. Notably, Prandtl’s estimation assumes a flow with a zero pressure gradient, which is of course not the case for a cylinder in cross-flow. However, the estimate does give a reasonable approximation for the upper bound of the RANS region when designing the grid.

Due to the relatively small diameter of the cylinders, the cell spacing circumferentially along the cylinder wall competed with the wall normal spacing for the boundary layer mesh. In order to adequately capture flow gradients resulting from the curvature of the cylinders, an increased number of grid points were placed along

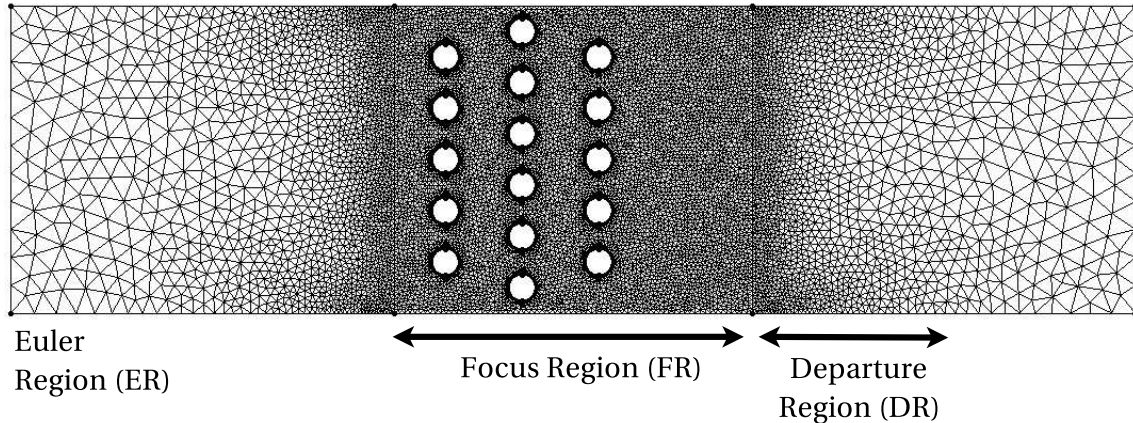


Figure 3.2: DES Cylinder Array, 9.9 million cells

the wall which lowered the aspect ratio of the cells in the RANS region. The lower aspect ratio reduced the anisotropy of the RANS cells which in turn brought the LES transition closer to the cylinder surface. Another competing factor was the hexahedral to tetrahedron transition. Tetrahedrons were intended for the domain outside of the boundary layer. To reduce high skewness and the associated grid metric errors, hexahedrons with aspect ratios of order one were desired at the boundary between hexahedral and tetrahedral cells. Resolution of these competing factors resulted in boundary layer hexahedrons growing significantly past δ_{99} and into the LES region, which forced some degree of anisotropy to be accepted for the LES.

The Focus Region (FR), defined in Section 2.3.3 and delineated in Figure 3.2, is characterized by fine, isotropic cell spacing designed for the LES branch of DES. On the cylinder array mesh, the FR extended two diameters ($2D$) upstream of the first row of cylinders and six diameters ($6D$) downstream of the last row of cylinders. The same FR proportions were also applied to the single cylinder grid. Selection of the FR objective grid density, Δ_0 , is discussed in Section 3.4.1.

3.4.1 Space/Time Coupling. Arriving at a Δ_0 suitable for capturing the necessary flow physics without exceeding the capabilities of the available computing resources required balancing spatial and temporal concerns. Based on an expected

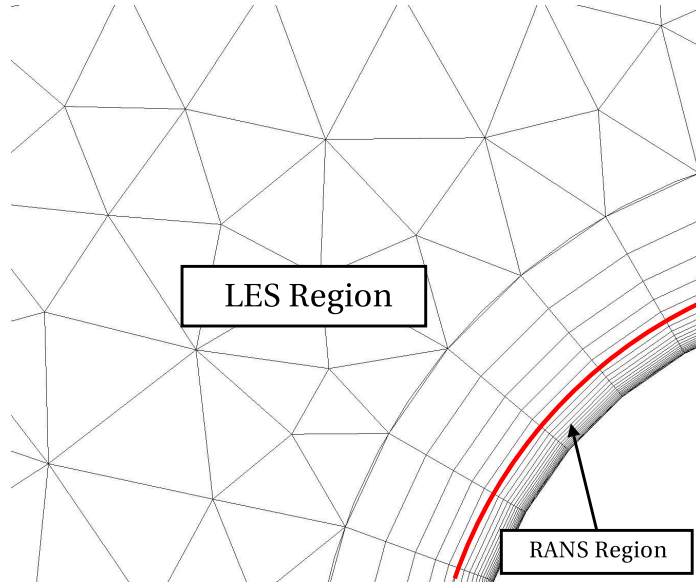


Figure 3.3: RANS-LES Transition, $y_{norm} = 0.065$ for the 14 million cell grid

Strouhal number of 0.2, the frequency of the bulk shedding is on the order of 8 Hz for the 1 m/s case and on the order of 40 Hz for the 5 m/s case. Spalart’s guidance for estimating the time step given by Equation (2.11) suggests ambitious timesteps of $\Delta t = 0.04$ s for the 1 m/s inlet case and $\Delta t = 0.015$ s for the 5 m/s inlet case based on $\Delta_0 = 0.2$. Determining the physical timestep of a CFD solver essentially sets the sampling rate thereby presetting the highest discernible spectral content of the data. The Nyquist sampling rate, given by $2f$ where f is the frequency of a desired signal, dictates the minimum sampling rate required to resolve f . Consequently, utilization of more conservative timesteps, $\Delta t = 0.01$ and $\Delta t = 0.005$, provided better resolution of the expected flow physics. Timesteps such as these yield sampling rates equivalent to 100 Hz for the 1 m/s case and 200 Hz for the 5 m/s case.

In the end, the grid density for the single cylinder and the 9.9 million cell grids was $\Delta_0 = 0.2$, a compromise between sampling the flow physics and conserving computational time. The fine, 14 million cell grid, which halved Δ_0 to 0.1 in the Focus Region, was constructed for testing grid convergence to ensure the numerical solution was independent of grid density. [21]

Figure 3.3 illustrates the RANS-DES transition at $y_{norm} = 0.065$, based on the 14 million cell grid where $\Delta_0 = 0.1$. Since Δy (wall-normal) in the boundary layer is very small compared to Δx (circumferential) and Δz (span-wise), the circumferential and span-wise spacing drive the LES transition point. In the case of the 14 million cell grid, $\Delta x = 0.0877$ and $\Delta z = 0.1$ (based on Δ_0), and the local grid density is computed by $\Delta = \max(\Delta x, \Delta y, \Delta z) = 0.1$. Thus, the RANS to LES transition point occurs when $C_{DES}\Delta = 0.065 < d_w$.

3.5 *Fluent Setup*

This section discusses the basic setup for the CFD solver, *Fluent*TM 6.2.16, for both RANS and DES.

Once the grid design was completed in *Gridgen*TM, it was exported to a *Fluent*TM case file. Case files contain the grid geometry, grid points, boundary conditions, and solver information. After starting the appropriate version of *Fluent*TM, serial 2-D/3-D double precision, a grid check was conducted followed by a series of smooth/swap cycles to reduce skewness and improve grid quality. To ensure the solver interpreted the correct dimensions of the grid geometry, the grid was scaled by inputting the units used to create the grid. Following these grid operations, the case file was saved and *Fluent*TM was restarted using the parallel mode to enable grid partitioning.

Depending on the availability of processors on the Beowulf cluster, the nominal 9.9 million cell grid was partitioned into twelve to sixteen partitions using the Metis method. The 14 million cell convergence grid was partitioned for twenty processors and the single cylinder case with 2.2 million cells was partitioned for four processors.

Even though the Navier-Stokes equations comprise a set of nonlinear, coupled equations, the Segregated Solver in *Fluent*TM solves the governing equations sequentially and segregated from one another. In the incompressible, ideal gas realm, the absence of strong gradients resulting from shocks allows faster convergence with an iterative sequential solver than with a simultaneous, coupled solver. *Fluent's*TM pro-

cedure for sequentially solving the governing equations is as follows. First, the fluid properties are updated throughout the domain; if the solver is on the first iteration, the initialized fluid properties are used. Next, the velocity field is updated by solving the momentum equations for u , v , and w using the current values of pressure and mass flux at cell faces. Because the fluid is set to ideal, incompressible gas, density is not explicitly solved as a conserved variable. To ensure continuity is satisfied, *Fluent*TM uses a pressure-correction method to adjusted the velocity field to balance mass-fluxes at cell faces. With the corrected velocity field, scalar equations such as energy and turbulence are solved. Finally, a convergence check is accomplished; if the solution is not converged, the solver continues to iterate. [9]

When employing an ideal gas assumption with $M \ll 1$, the changes in pressure throughout the solution are very small. This increases the solution's susceptibility to round-off error. To combat the round-off error, the Operating Pressure was set to the free-stream pressure of 101,325 *Pa*, allowing *Fluent*TM to solve for gage pressure, the difference between local static pressure and operating (reference) static pressure. [9]

Often overlooked, solver boundary conditions deserve consideration in this section. The computational domain was essentially a wind-tunnel model: a rectangular prism with inlet and outlet planes at opposite ends of the tube. *Fluent's*TM Velocity Inlet boundary condition, specifically designed for low-speed incompressible flows, was invoked at the inlet plane. At the Velocity Inlet boundary condition, scalar quantities such as velocity components, temperature, and modified turbulent viscosity were specified while stagnation values were allowed to float and normalize to the velocity distribution. For a cell adjacent to a Velocity Inlet, *Fluent*TM computed the momentum and energy fluxes across the cell face normal to the boundary with the user's velocity inputs. [9] On the outlet plane, an Outflow boundary condition was applied. Outflow boundaries are suitable when the velocity and pressure at the outlet are unknown and downstream conditions do not significantly impact the upstream flow dynamics. *Fluent*TM handled the Outflow boundaries with a simple extrapolation from the grid interior. Finally, the walls of the tunnel were modeled as slip walls.

This was accomplished in *Fluent* by specifying zero shear stress under the Momentum panel for a Wall boundary condition. The Wall boundary condition at the cylinder surface used the default No-Slip condition for the wall shear thereby setting the modified turbulent viscosity, $\tilde{\nu}$, equal to zero. Note that since the grid is sufficiently fine to resolve the laminar sublayer ($y^+ = 1$ for Spalart-Allmaras turbulence model), the shear stress computation at the wall used the inner law relationship

$$\frac{\bar{u}}{v^*} = \frac{yv^*}{\nu} \quad (3.3)$$

where v^* is the friction velocity given by

$$v^* = \left(\frac{\tau_w}{\rho} \right)^{\frac{1}{2}} \quad (3.4)$$

and \bar{u} is the mean velocity parallel to the wall, y is the normal distance from the wall, ν is the kinematic viscosity, and τ_w is the shear stress at the wall. The thermal condition for both No-Slip and Slip Walls was set to zero heat flux at the cylinder wall. [9, 28]

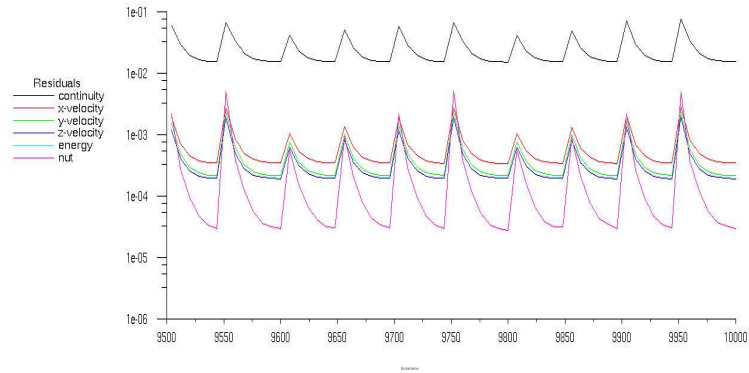
3.5.1 RANS Specific Setup. For RANS computations, the turbulence model was set to Spalart-Allmaras on the Viscous panel and all default values were accepted. The Segregated Solver was set to use a second-order upwind discretization for momentum, energy, and modified turbulence viscosity achieved by applying a Taylor series expansion of these cell-centered quantities about the cell centroid. Finally, execution of a RANS computation was accomplished by initializing the entire domain to the inlet (free-stream) conditions and iterating until convergence was achieved. The convergence criteria for continuity, velocity, and turbulent viscosity was set at three orders of magnitude. However, lift and drag on the cylinder array were often used to quantify convergence to steady state. A steady-state solution was possible because the unsteady shedding phenomena associated with bluff body flow were substantially damped by the Spalart-Allmaras RANS turbulence model.

3.5.2 Detached-Eddy Simulation Specific Setup. Once a steady-state solution was attained using strictly RANS methods, the DES turbulence model was selected on the Viscous panel. This action automatically set the solver to an unsteady, second-order temporal discretization employing a bounded, central-difference discretization of the momentum equation. The default DES constant of $C_{DES} = 0.65$ suggested by Spalart was accepted. The Spalart-Allmaras turbulence model is used exclusively as the RANS model for a DES in *Fluent*TM 6.2.16.

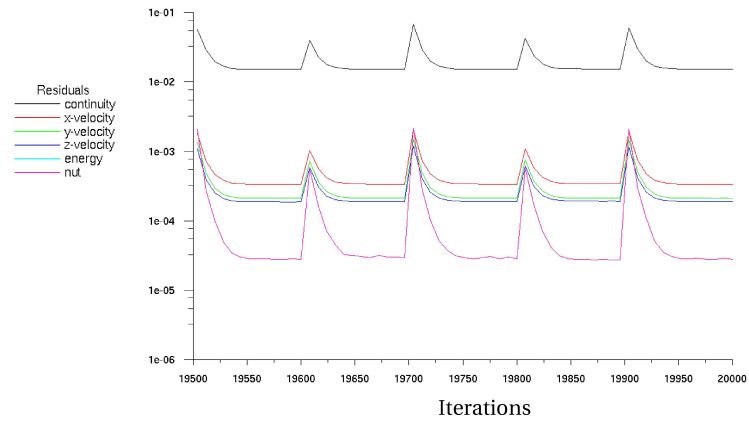
Finally, when using *Fluent*'sTM implicit solver, which employs dual time-stepping, the maximum number of sub-iterations for each physical time step must be determined. Essentially, each time step is a steady-state computation and should be sufficiently converged before incrementing the physical time step. A sub-iteration convergence study using the 9.9 million cell grid was conducted to determine an appropriate maximum number of sub-iterations for the solver during DES. Figure 3.4 shows residual plots over several timesteps. The residuals begin to show asymptotic behavior after 50 sub-iterations. However, for 100 sub-iterations per timestep, the residuals were completely asymptotic. Thus, during data collection runs, 70 sub-iterations was deemed more than sufficient.

3.6 Visualization Tool Kit and Post-Processing

Large grid sizes and small timesteps lead to significant data storage and post-processing burdens. *Fluent*TM Data files for a single time step contain the flow properties at every point in the grid and ballooned in size to 2.9 Gigabytes for the 14 million cell grid. Using *Fluent*'sTM built-in data output format, collecting four seconds of time-accurate data for a single case would require approximately 1.1 Terabytes. An alternative to *Fluent*'sTM data storage method was the Fluent VTK Extractor (FVE) which directly accesses data from the *Fluent*TM arrays at runtime and outputs user-specified geometry and data to a Visualization Tool Kit (VTK) XML file. [15] VTK is an open source, 3-D graphics, image, and visualization software application which



(a)



(b)

Figure 3.4: Residual Output, 9.9M cell grid, 1 m/s inlet velocity (a) 50 Sub-iterations per timestep (b) 100 Sub-iterations per timestep

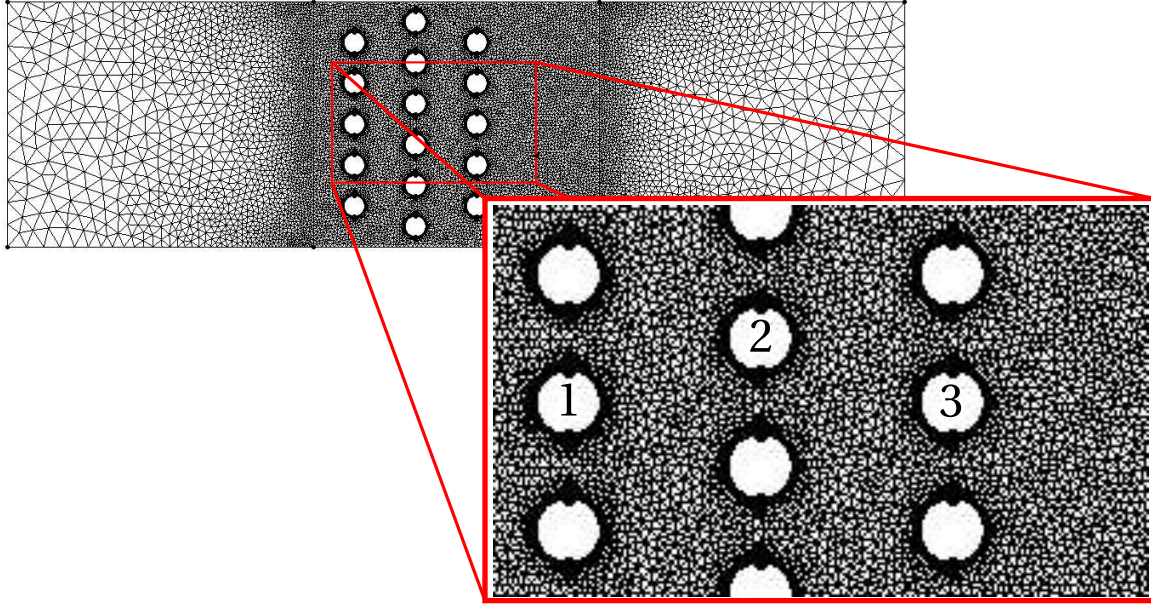


Figure 3.5: VTK bounding box; only data inside the box is stored at runtime; boundary layer and Strouhal number were computed for the numbered cylinders

supports scalar, vector, and tensor operations, as well as mesh smoothing and cutting functions for filtering data. [20]

The FVE is implemented as a *Fluent*TM User-Defined, Compiled Function. The user first creates C functions containing instructions for specifying bounding boxes, cut-planes, and point probes used to sample scalars of interest such as pressure, density, and velocity at runtime. The C file and compiled FVE libraries are selected on the *Fluent*TM Compiled Functions menu and then subsequently built and loaded. Finally, at runtime, *Fluent*TM calls the FVE user-defined function and outputs a VTK format data file for each time step. This method saved tremendous storage space since only regions of interest in the grid are stored, and the number of scalars in the output is reduced to those selected by the user. Data storage savings of up to 99% and runtime reductions of up to 15% are possible when using FVE. [15] Figure 3.5 illustrates the size and location of the data subset saved at runtime using FVE.

Because the fluid is an incompressible, ideal gas formulation employing the Segregated Solver, density is treated as a constant. To minimize output, only static

pressure and x, y, and z velocity were chosen for output during DES. With these four scalars, virtually any other flow quantity can be computed during post-processing.

Because the simulation was run in parallel, the FVE utility wrote an output file for each partition of the grid at each time step. In order to view the entire dataset, the information must be stitched back together using a locally developed utility written in Python known as the *Fuser*. The *Fuser* uses VTK function calls to identify the shared nodes of each partition and output a single, unified grid and data set for visualization and data reduction.

Visualization of the VTK output was accomplished with MayaVi, an open-source visualization program written in Python. Using MayaVi, each of the stored scalars can be viewed and interpreted with a variety of techniques including cut-planes and point probes. [16] MayaVi is limited, however, as far as computing advanced flow dynamics such as vorticity and path lines in place. For this reason, a Python script, *vtk2ensight*, was developed to convert the VTK files to *Ensignt*TM format. *Vtk2ensight* uses VTK 5.0 to write each of the scalar arrays in the VTK output to time-accurate *Ensignt*TM data files.

*Ensignt*TM, a commercial engineering and scientific visualization application, is able to recognize transient data sets and import each time step into a single session. This allows the user to examine changes in the data over time using animation and particle path-lines. Furthermore, *Ensignt*TM has the ability to readily compute and visualize vorticity, velocity vectors, and other derived flow characteristics. [6]

Animations are an extremely powerful tool for garnering an understanding of unsteady flow dynamics. Thus, animated visualizations of derived variables such as velocity magnitude, velocity vectors, and vorticity were constructed using *Ensignt's*TM variable calculator and transient data flip-books. Path-lines, the locus of points describing the movement of a massless particles through an unsteady velocity field are another tool available inside *Ensignt*. Naturally, a visualization capability such as this was extraordinarily helpful in ascertaining mechanisms for droplet transport.

Examination of instantaneous data in the form of animations and path-lines is a valuable tool, however, time-averaged data considers long-period bulk motion. Computing time-averaged data required the development of another Python script with VTK function calls. The time-averaging utility read in each scalar array from VTK XML data files, summed the data, and divided by the number of timesteps before finally outputting the data to a new VTK XML file.

Determining spectral content in a flow at a point is the first step in computing the Strouhal number (Section 2.1). Extracting data collected via a point probe over time necessitated the development of another Python script. Scalar data from time-accurate VTK data files was interpolated from cell-centered quantities to a point requested by the user and written to an ASCII file. The resultant record of time-accurate data at a point in the flow, formatted as space-delimited ASCII, was then readily accessible to *Matlab*TM for performing spectral analysis and computing turbulence statistics. Power Spectral Density (PSD) plots of the data were created to compute the Strouhal number using Equation (2.1). Turbulence statistics such as mean velocity, RMS velocity, and turbulence intensity were also checked.

To conclude, the synthesis of time-accurate methods such as animated visualizations, path-lines, and spectral content combined with time-averaged data yielded the necessary tools to reduce and characterize the turbulent flow-field inside the cylinder array and search for explanations of droplet transport.

IV. Results

The results presented in this chapter summarize the outcome of RANS and Detached-Eddy Simulations from the standpoint of model validation and droplet transport mechanisms related to fire suppression. In the vein of model validation, the numerical simulations focused on boundary layer and vortex shedding physics for a single cylinder and an array of cylinders. Examination of the data from the perspective of droplet transport was conducted exclusively on the fine cylinder array grid.

4.1 *Single Cylinder DES Validation*

4.1.1 Boundary Layer Resolution. Data gathered from both RANS and DES methods supported the verification of the boundary layer profile. Wall y^+ , a non-dimensional parameter used to quantify the quality of near-wall grid spacing, was plotted for each case to confirm Spalart-Allmaras performance in the boundary layer. When using the Spalart-Allmaras equation to model the boundary layer and avoid wall-functions, the *Fluent*TM manual recommends y^+ values on the order of one or less at wall boundaries. [9] Figure 4.1 gives RANS and DES wall y^+ values for the single cylinder grid at $U_\infty = 1 \text{ m/s}$. Notably, $y^+ < 1$ was satisfied everywhere along the surface of the cylinder. Similarly, y^+ trends for the 5 m/s free-stream case were also observed.

In addition to inspecting y^+ , the curvature of the boundary layer profile was also qualitatively analyzed to assess the quality of the boundary layer model. Turbulent boundary layers along a line described by Figure 4.3 are clearly depicted in Figure 4.2, demonstrating adequate grid spacing. The results of the wall y^+ variables coupled with the boundary layer profiles offers sufficient evidence to accept the boundary layer as well-resolved and sufficient for computing an accurate numerical solution.

4.1.2 Spectral Content. Frequency data collected at a point described by Figure 4.4 was used to compute the Strouhal number for the single cylinder 2.2 million cell grid. The power spectral density (PSD) plot for the single cylinder case,

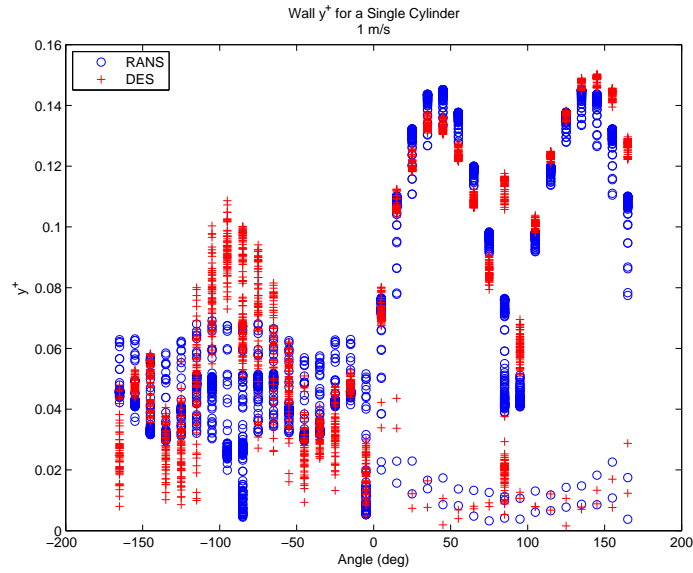


Figure 4.1: RANS and DES comparison of wall y^+ values for a single cylinder, $U_\infty = 1 \text{ m/s}$, 2.2 M cells

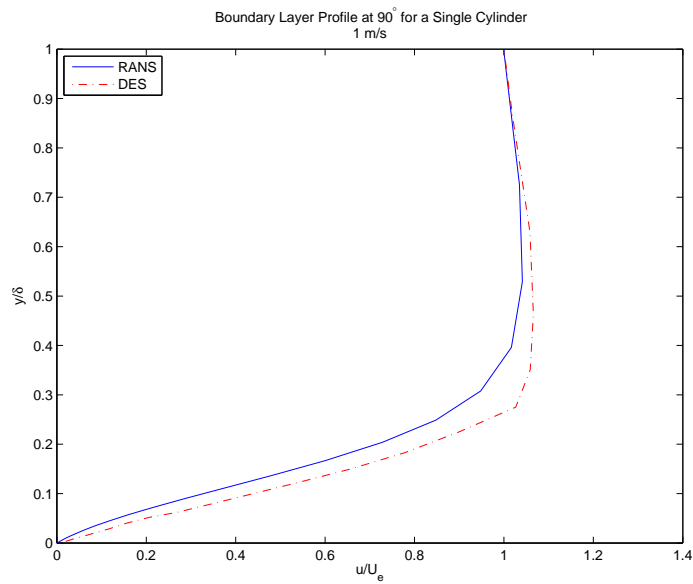


Figure 4.2: RANS and DES boundary layer profile comparison for a single cylinder at 90° , $U_\infty = 1 \text{ m/s}$, 2.2 M cells; Figure 4.3 describes the measurement location

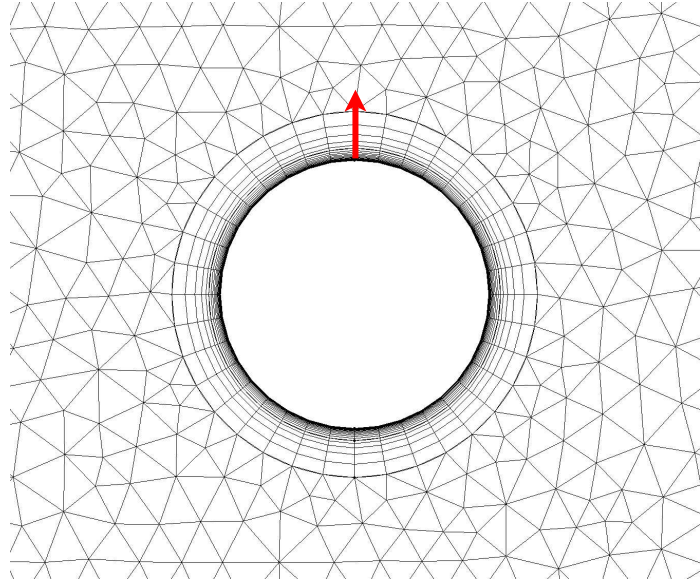


Figure 4.3: Boundary layer profile measurement location; the arrow describes the direction of increasing y_{norm}

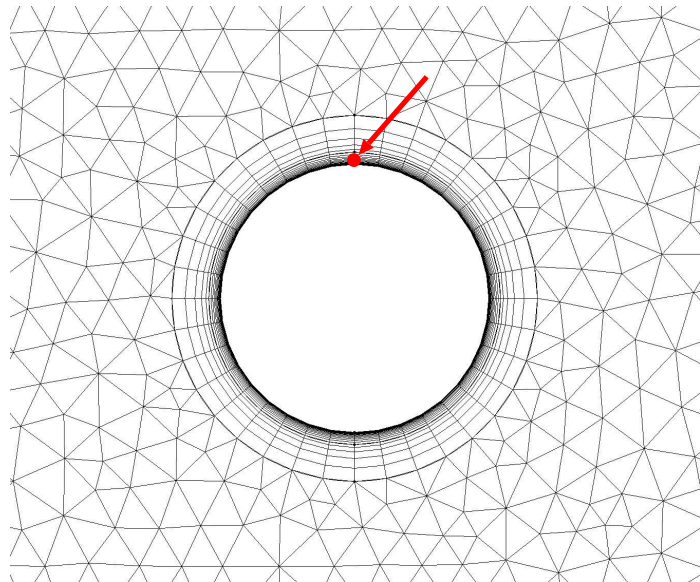
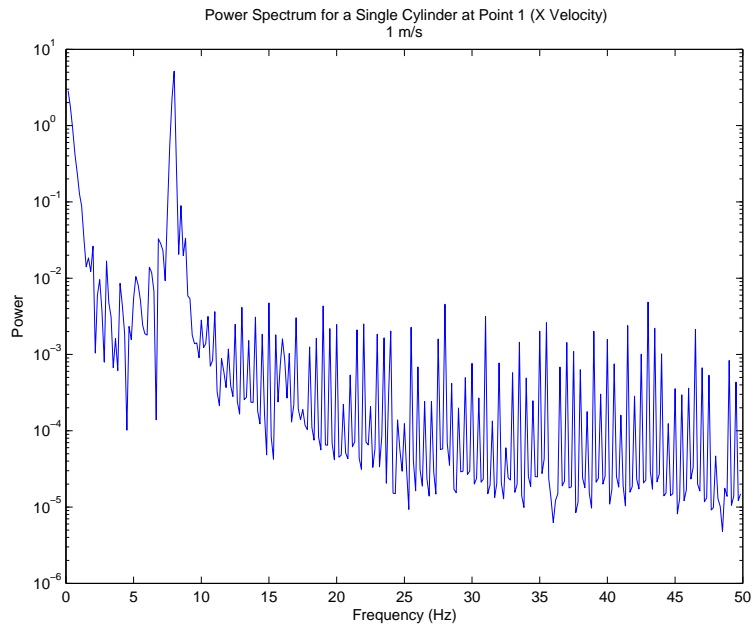
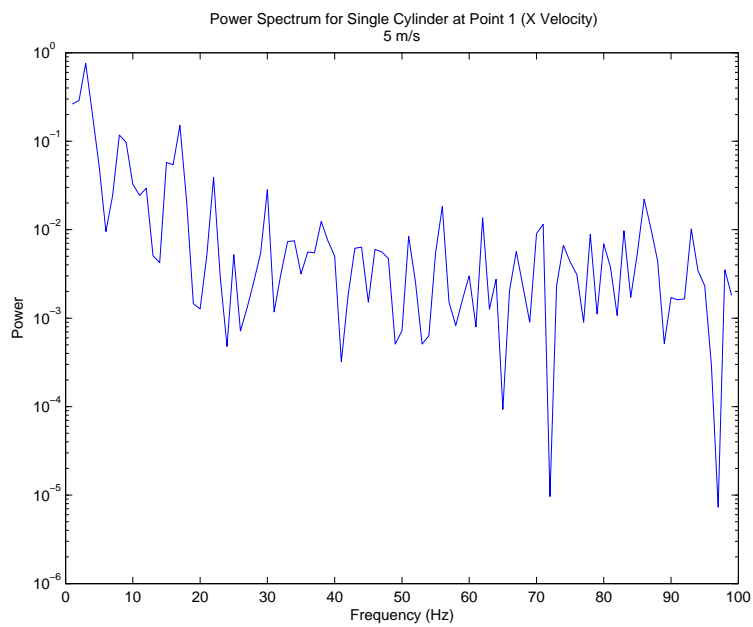


Figure 4.4: Frequency measurement location for computing Strouhal number



(a)



(b)

Figure 4.5: Power spectrum, single cylinder, 2.2 M cells (a) $U_\infty = 1 \text{ m/s}$ (b) $U_\infty = 5 \text{ m/s}$; Figure 4.4 describes the measurement location

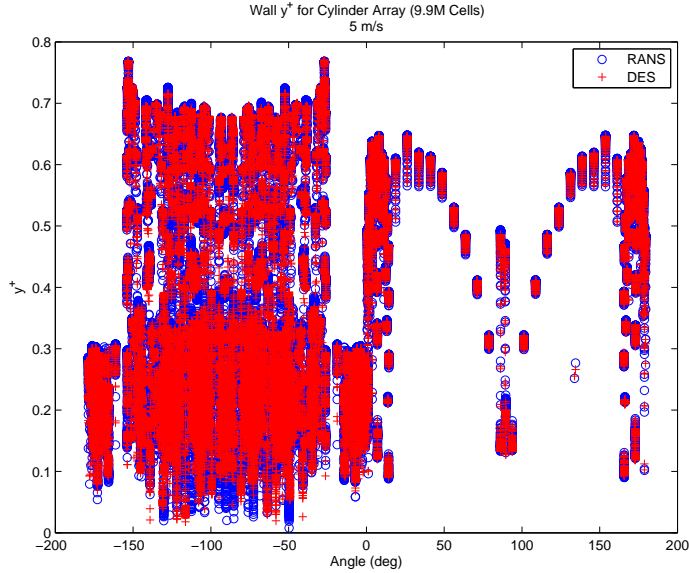


Figure 4.6: RANS and DES comparison of wall y^+ values, cylinder array, $U_\infty = 5 \text{ m/s}$, 9.9 M cells

Figure 4.5 (a), shows a strong peak at 8 Hz corresponding to a Strouhal number of $St = 0.203$ ($Re = 1,575$) matching nicely with the accepted value of $St = 0.2$ for $100 < Re < 10^5$. The higher speed case, $U_\infty = 5 \text{ m/s}$, depicted in Figure 4.5 (b) provides no obvious shedding frequency indicating the grid was too coarse to adequately capture the higher frequency mode associated with a faster free-stream velocity. While the single cylinder grid was not refined to resolve the shedding in the high speed case, the results influenced the refinement of the cylinder array grid to ensure shedding was captured.

4.2 Exploration of the Circular Cylinder Array

4.2.1 Boundary Layer Resolution. Investigation of boundary layer behavior on the cylinder array grids was accomplished in the same manner as the analysis performed on the single cylinder grid. A plot of y^+ values for the cylinder array is given in Figure 4.6. Although the figure is crowded, the the maximum wall y^+ values are the key feature exhibited by the plot. Once more, the Spalart-Allmaras criteria of wall $y^+ < 1$ was met throughout the array.

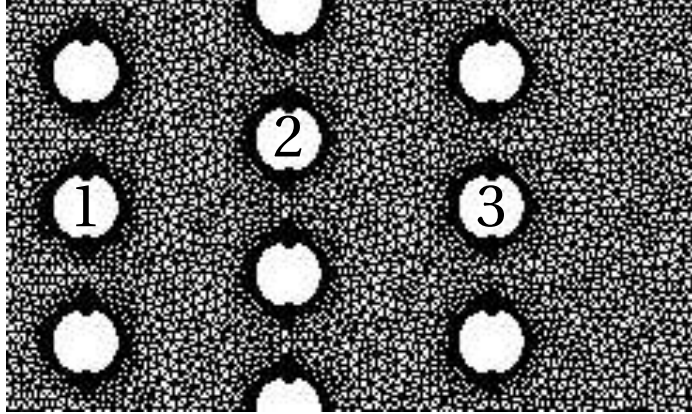
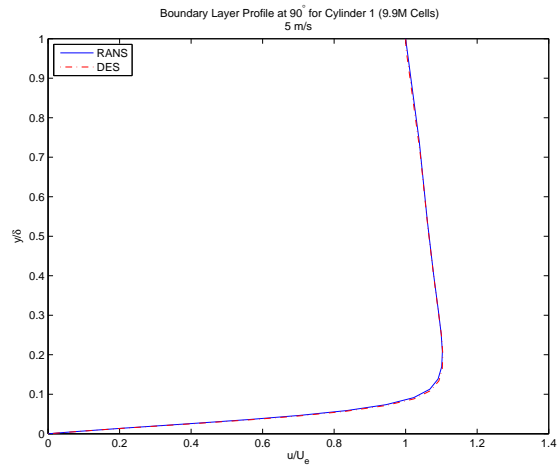


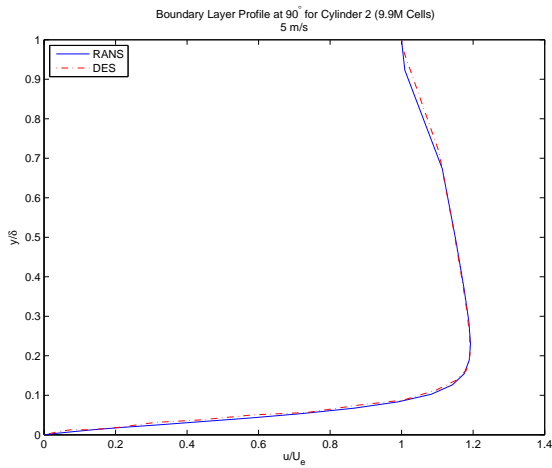
Figure 4.7: VTK bounding box illustrating the designation of certain cylinders in the array

Figure 4.8 qualitatively compares the boundary layer profiles of Cylinders 1, 2, and 3 designated in Figure 4.7, taken along a line described by Figure 4.3. Like the single cylinder case, the boundary layer velocity profiles at $U_\infty = 5 \text{ m/s}$ on the 9.9 million cell array grid presented well-captured turbulent velocity profiles. Since the variation of free-stream velocity and grid density did not appreciably influence the behavior of the boundary layer, only a single case was illustrated in Figure 4.8.

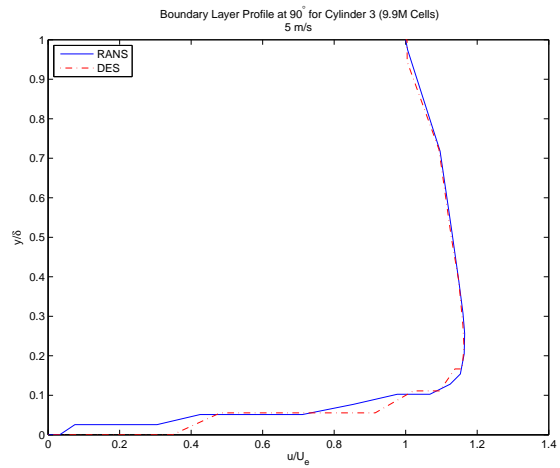
4.2.2 Spectral Content. Even though the Strouhal number corresponding to a circular cylinder in an array is not correlated to Reynolds number in the same way as it is for a single cylinder, the frequency content and Strouhal number for Cylinder 1 were nonetheless computed at a point indicated in Figure 4.4. Cylinder 1 was chosen because the oncoming flow is free-stream, unlike the flow seen by Cylinders 2 and 3, which lie in the unsteady, turbulent wakes of the upstream cylinders and experience mean local flow velocities as high as twice the free-stream. The PSD plots of Figure 4.9 from the 9.9 million cell grid revealed a faint peak near 6 Hz for $U_\infty = 1 \text{ m/s}$ and no discernible shedding frequency for $U_\infty = 5 \text{ m/s}$. The lack of a shedding frequency for the 5 m/s free-stream case indicates that the 9.9 million cell grid was too coarse to detect the flow physics of interest. Nevertheless, the enhanced spatial resolution of the 14 million cell grid satisfactorily captured the Karman vortex shedding which



(a)

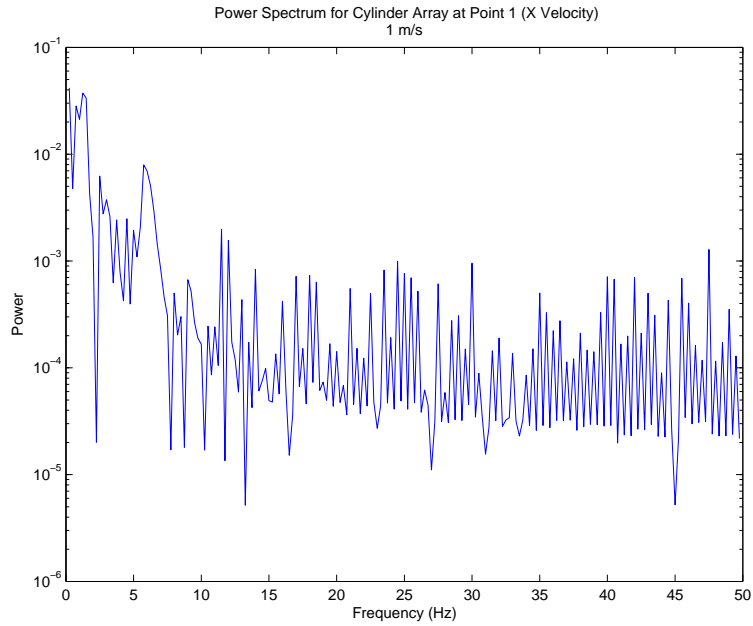


(b)

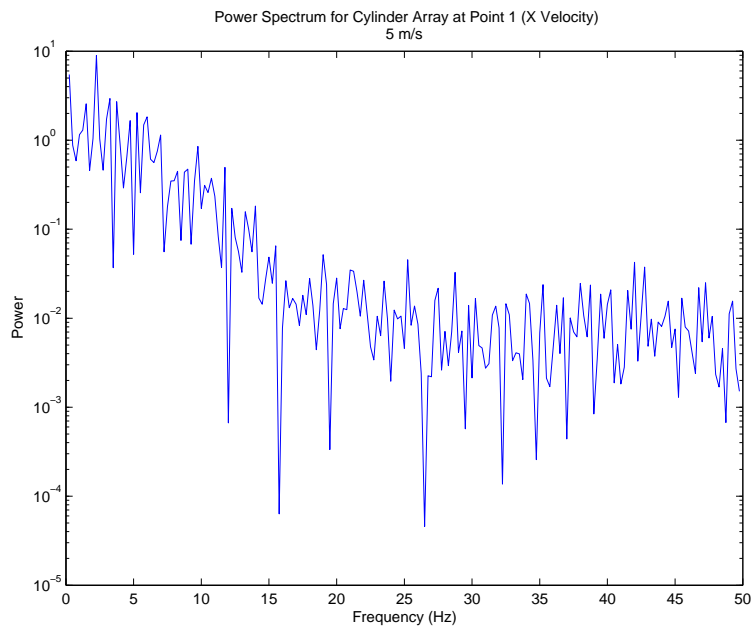


(c)

Figure 4.8: RANS and DES cylinder array boundary layer profile comparison at 90° , $U_\infty = 5 \text{ m/s}$, 9.9 M cells; Figure 4.3 describes the measurement location; (a) Cylinder 1 (b) Cylinder 2 (c) Cylinder 3

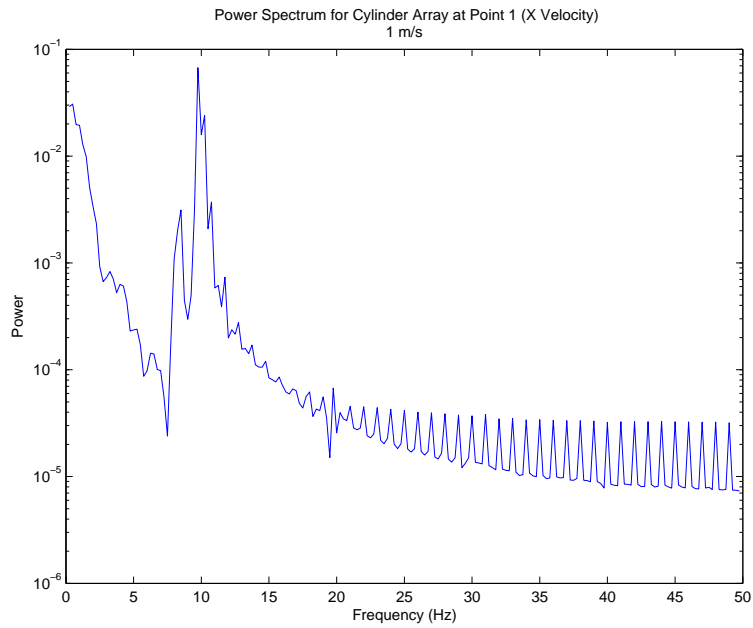


(a)

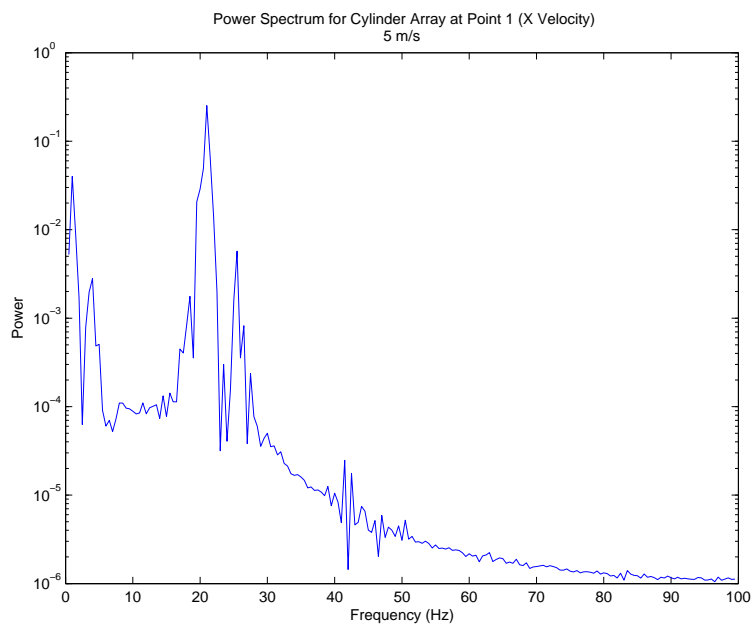


(b)

Figure 4.9: Power spectrum, cylinder array at cylinder 1, 9.9 M cells (a) $U_\infty = 1 \text{ m/s}$ (b) $U_\infty = 5 \text{ m/s}$; Figure 4.4 describes the measurement location



(a)



(b)

Figure 4.10: Power spectrum, cylinder array at cylinder 1, 14 M cells (a) $U_\infty = 1 \text{ m/s}$ (b) $U_\infty = 5 \text{ m/s}$; Figure 4.4 describes the measurement location

is evident in the power spectrum plots of Figure 4.10. At $U_\infty = 1 \text{ m/s}$, a 10 Hz signal dominates the flow, and at $U_\infty = 5 \text{ m/s}$, a 20 Hz peak represents the shedding frequency. Strouhal numbers based on the 14 million cell grid data were computed at $U_\infty = 1 \text{ m/s}$ and $U_\infty = 5 \text{ m/s}$ to be $St = 0.25$ and $St = 0.11$ respectively. The deviation from the accepted $St = 0.2$ for a single cylinder is likely due to influence of adjacent cylinders shedding asynchronously with Cylinder 1.

The results of the power spectral density plots of the single cylinder and the cylinder array demonstrated that the objective cell spacing of $\Delta_0 = 0.2$ in the LES region was insufficient to describe the primary flow physics of interest. Although the 14 million cell mesh was intended to investigate solution grid-independence, the simulation remained a success because the 14 million cell grid enabled the study of droplet transport mechanisms.

4.3 Droplet Transport Mechanisms

Initially, the search for droplet transport and trapping mechanisms focused on span-wise flow and vortices capable of entraining particles. The first hypothesis put forth in Section 1.3 contended that non-uniform, span-wise shedding generated waves pushing entrained droplets toward the side walls of the tunnel. After deposition on the walls, the droplets would drip and pool on the tunnel floor.

Strong, non-uniform shedding along the span of a single cylinder is typically manifested by the pinching and folding of vortex cores in the wake illustrated by Figure 4.11. For the single cylinder case, weak, non-uniform shedding was observed and is depicted in Figure 4.12 and Figure 4.13. As time progresses, the vortex core represented by (a) and (b) in Figure 4.12 bends and separates into two distinct vortex cores at (c) and (d) causing weak span-wise flow to develop briefly. The y-velocity contours shown in Figure 4.13 correspond to the the vortex core evolution in Figure 4.12. The y-velocity plots, taken $0.25D$ downstream of the cylinder, depict weak asynchronous span-wise shedding. As (a) and (b) of Figure 4.13 are trending down, (d) and (e) indicate the opposite. While the non-uniform shedding and span-wise

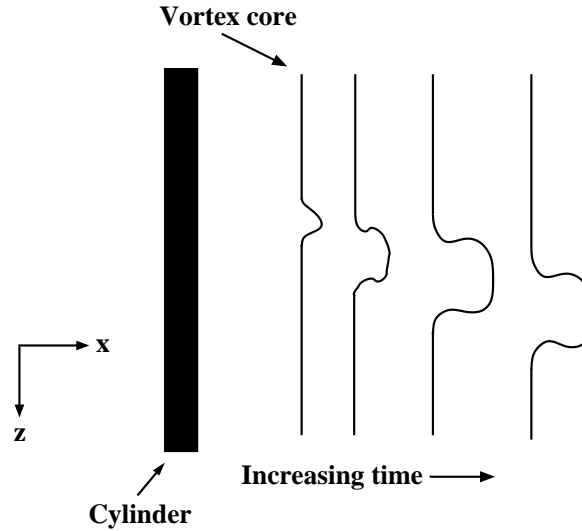


Figure 4.11: Expected vortex core time evolution during strong, non-uniform, span-wise shedding

vorticity of the single cylinder case was detectable, the span-wise flow was quite weak and not capable of supporting span-wise droplet transport.

The same analysis of vortex cores and y -velocity distribution on the cylinder array grid yielded no evidence whatsoever of span-wise vorticity or non-uniform shedding. Figure 4.14 shows a vortex core computation representative of the cylinder array which is remarkably more uniform and stratified than that single cylinder case. Y -velocity plots on a cut-plane $0.25D$ downstream of the second row of cylinders (Figure 4.15) further reinforces the absence of non-uniform shedding and the lack of span-wise flow inside the array. In fact, there is almost no change in the y -velocity distribution along the span of the cylinders. The close proximity of the cylinders seems to force the vortex cores to remain aligned with the cylinder span. Thus, span-wise droplet transport toward the tunnel walls was not witnessed using this model for the conditions specified.

4.3.1 Particle Transit Time Analysis. With the span-wise motion hypothesis disproved, the second hypothesis described in Section 1.3 was explored. A first-order inertial estimate, originally discussed in Section 2.4.1, was conducted using data

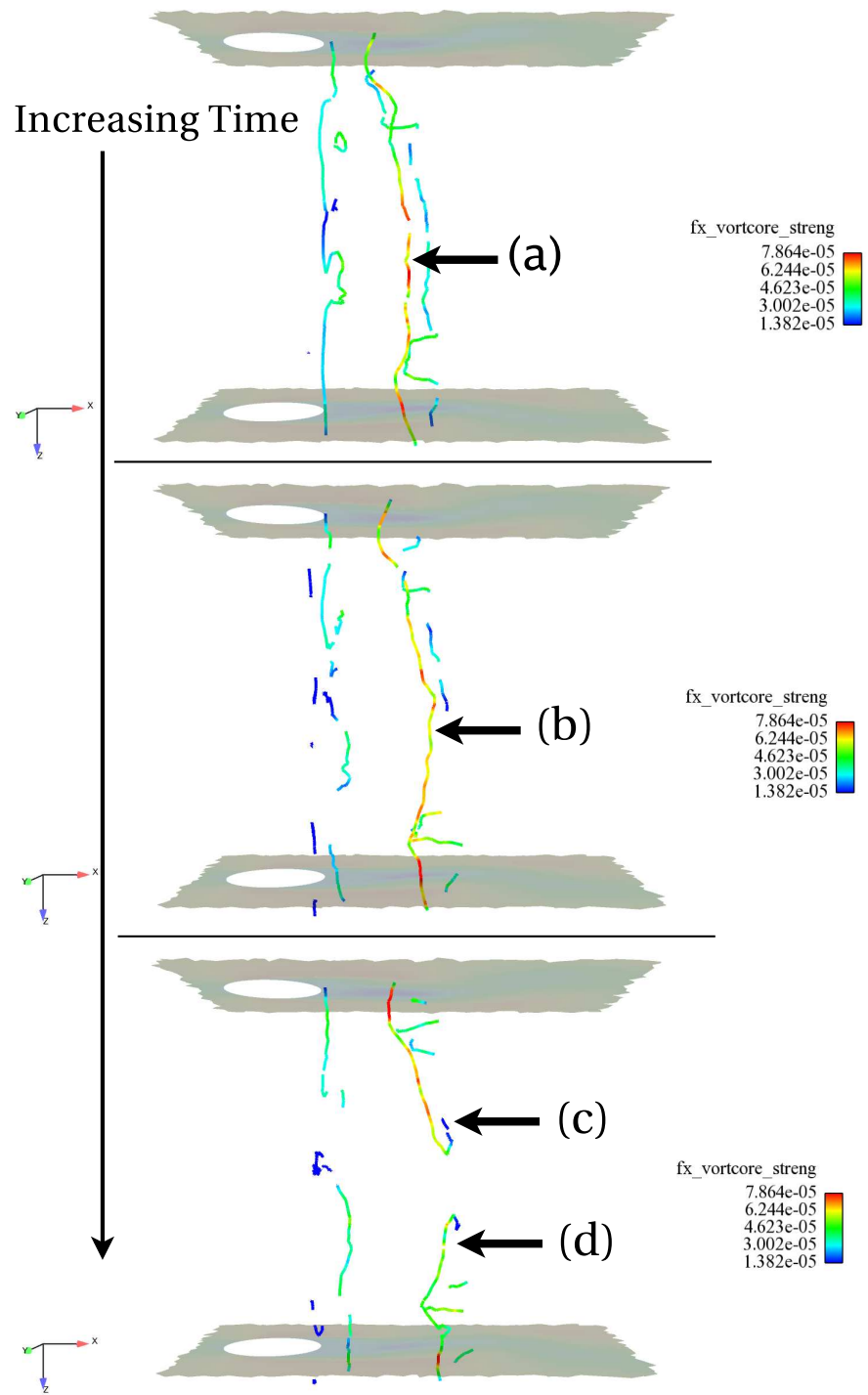


Figure 4.12: Vortex core time evolution during weak, non-uniform, span-wise shedding, single cylinder, $U_\infty = 1 \text{ m/s}$

Increasing Time

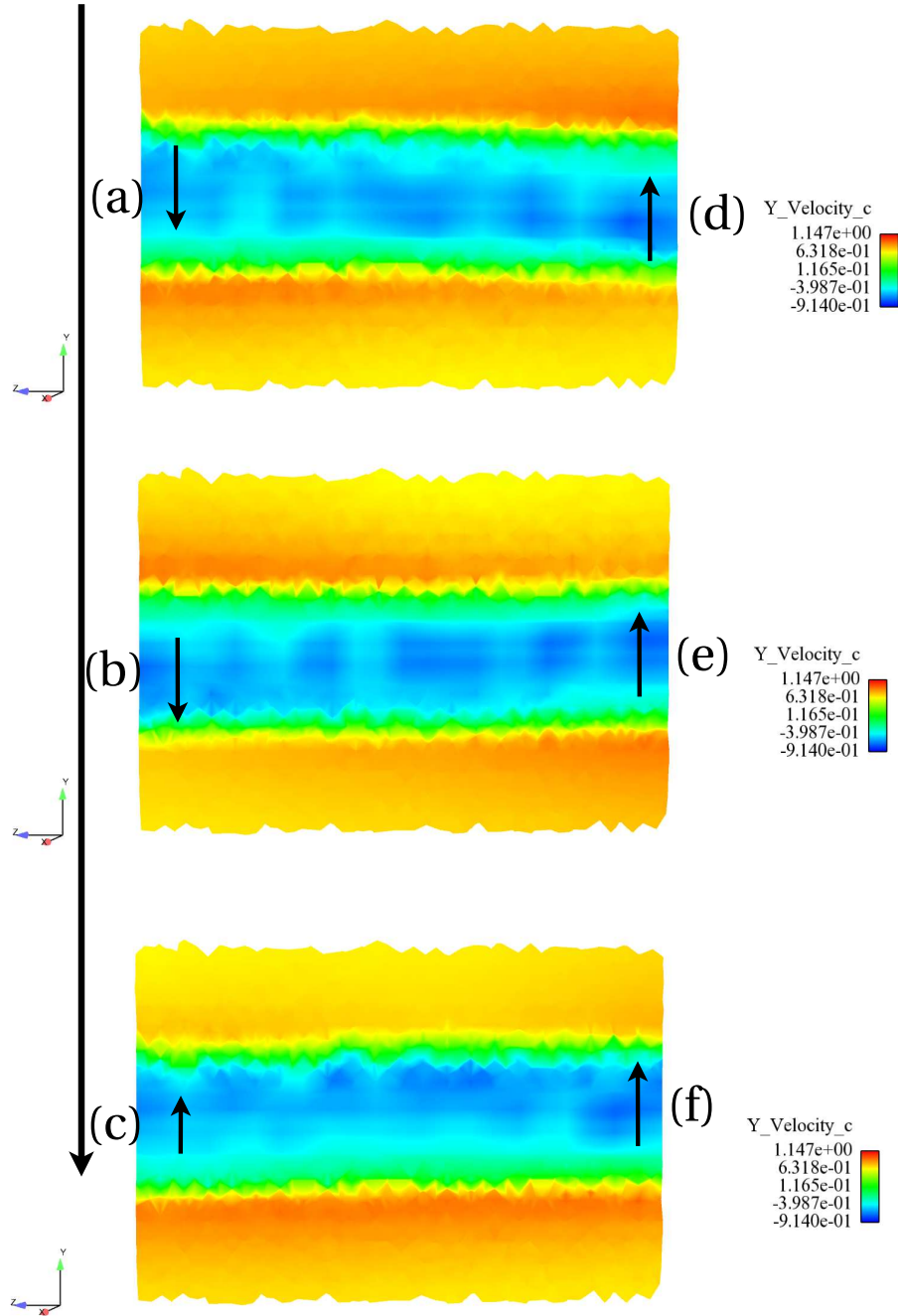


Figure 4.13: Y-Velocity visualization, $U_\infty = 1 \text{ m/s}$, single cylinder, $x = 0.25D$

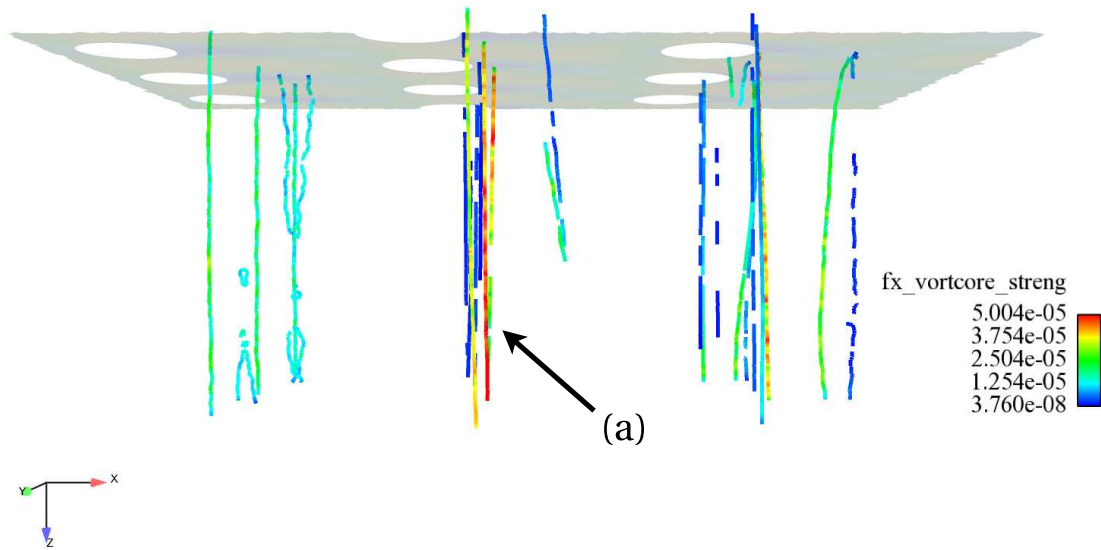


Figure 4.14: Instantaneous vortex core visualization, $U_\infty = 1 \text{ m/s}$, cylinder array, 14 M cells

from the 14 million cell grid Detached-Eddy Simulations. In the most conservative case, a droplet could fall as far as 1 *inch* (0.0254 *m*), the vertical distance between cylinders in the same row, before impacting the clutter. For the 1 *m/s* free-stream case, the average carrier fluid velocity in the spaces between the cylinders of the array was approximately 1.75 *m/s*. Applying only the acceleration of gravity to the droplet, the time required for a droplet to fall and impact another cylinder was $t = 0.072 \text{ s}$. However, at a mean velocity of 1.75 *m/s* the time required for a particle to traverse 7 *inches* (0.1778 *m*), the horizontal dimension of the array, was $t = 0.10 \text{ s}$. Thus, the likelihood of a droplet impacting one of the cylinders before exiting the array was quite high in the low-speed case. In contrast, the average velocity between the cylinders for the 5 *m/s* free-stream case was 8.5 *m/s*. A droplet entrained in this flow could negotiate the array in approximately $t = 0.02 \text{ s}$, which is 3.6 times faster than the time required for the same particle to fall into another cylinder. Although this analysis is quite simple, it indicates that velocity and inertia play the dominating role in governing whether or not an entrained particle impacts a cylinder or is whisked through the clutter.

Increasing Time

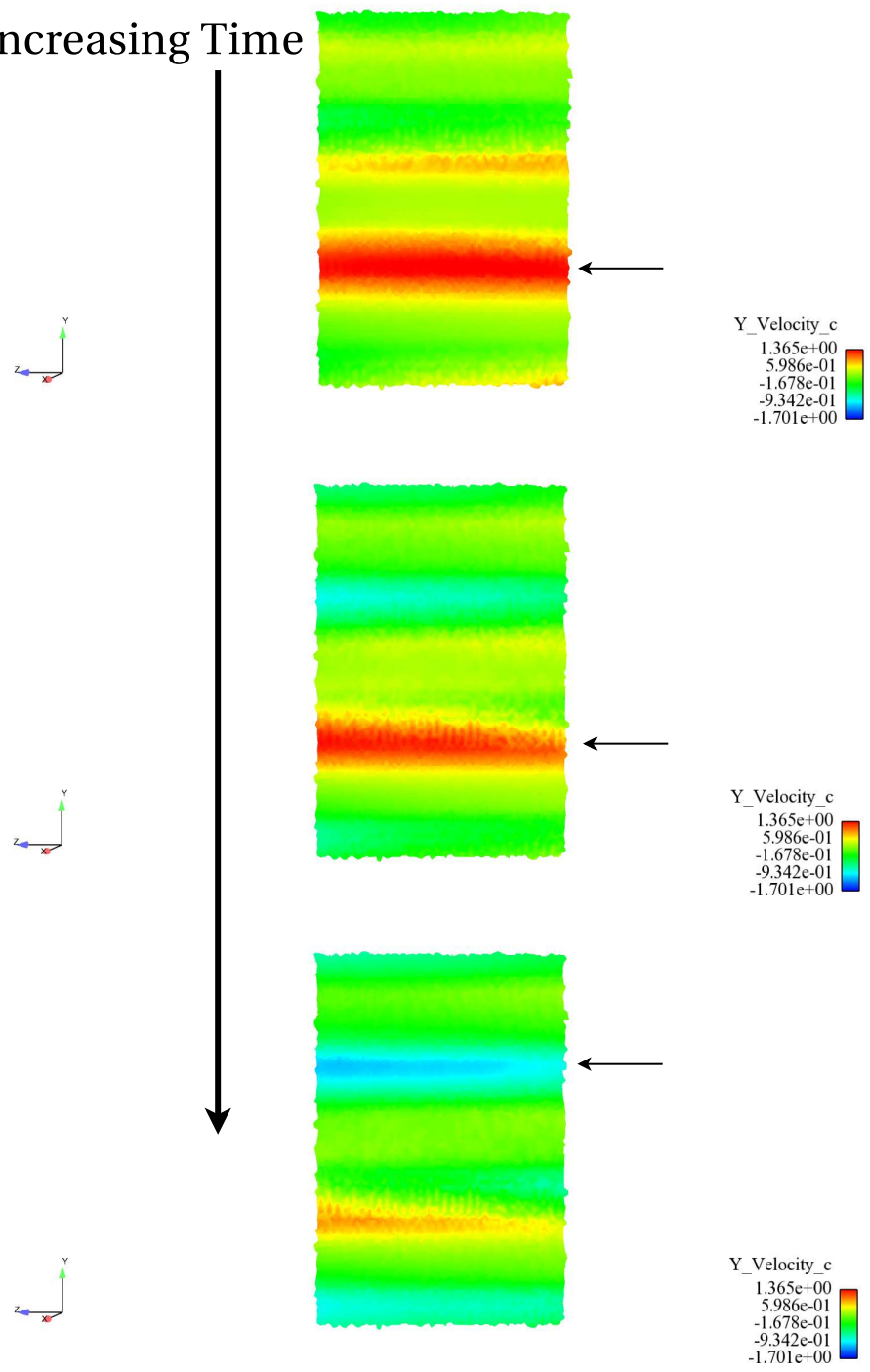


Figure 4.15: Y-Velocity visualization, $U_\infty = 1 \text{ m/s}$, cylinder array, $x = 0.25D$, 14 M cells

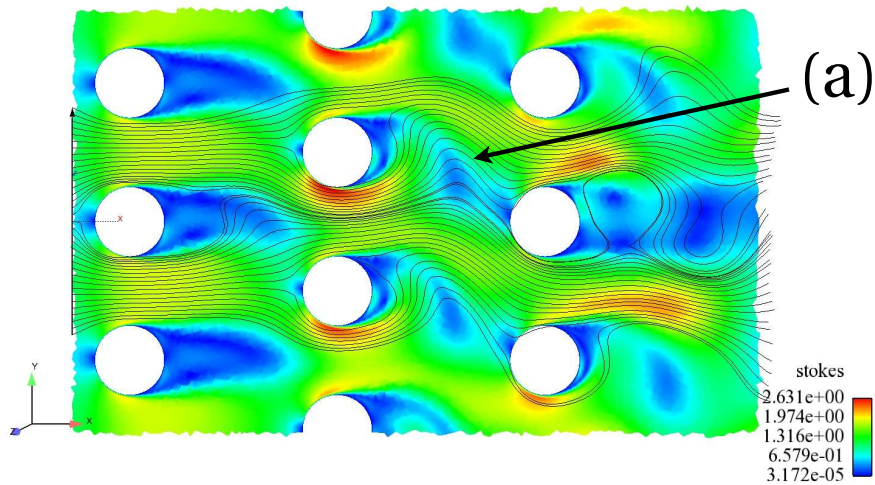


Figure 4.16: Streamline and Stokes number visualization at simulation $t = 3.77 \text{ s}$, $U_\infty = 1 \text{ m/s}$, cylinder array, 14 M cells

4.3.2 Stokes Number Analysis. Investigating whether or not the droplets were likely to impact the clutter based on unsteady phenomena as well as the time-averaged flow characteristics was accomplished by composing animations of streamlines superimposed on contour plots of Stokes number. This was inspired by the discussion of Section 2.4.2 which described the effect of Stokes number on entrained particle motion. The Stokes number computation assumed water droplet particles of approximately $90 \mu\text{m}$ in diameter, a likely size for droplets emanating from a spray nozzle. [9]

Figure 4.16 contains a representative instantaneous Stokes number contour plot with streamlines superimposed for the 1 m/s free-stream case. Overall, the Stokes number throughout the flow-field depicted in Figure 4.16 is relatively low. Much of the flow between the cylinders is colored green which corresponds to Stokes numbers on the order of one; also the peak Stokes number of the flow, $Stk = 2.6$, is relatively low. The vortex shedding of the cylinders in Figure 4.16 induced significant streamline curvature in the wake where the corresponding Stokes number is on the order of one or less indicating that any dispersed particles would likely track along the streamlines. Furthermore, streamlines in the low-speed case illustrated by Figure 4.16 (a) pass

Increasing Time

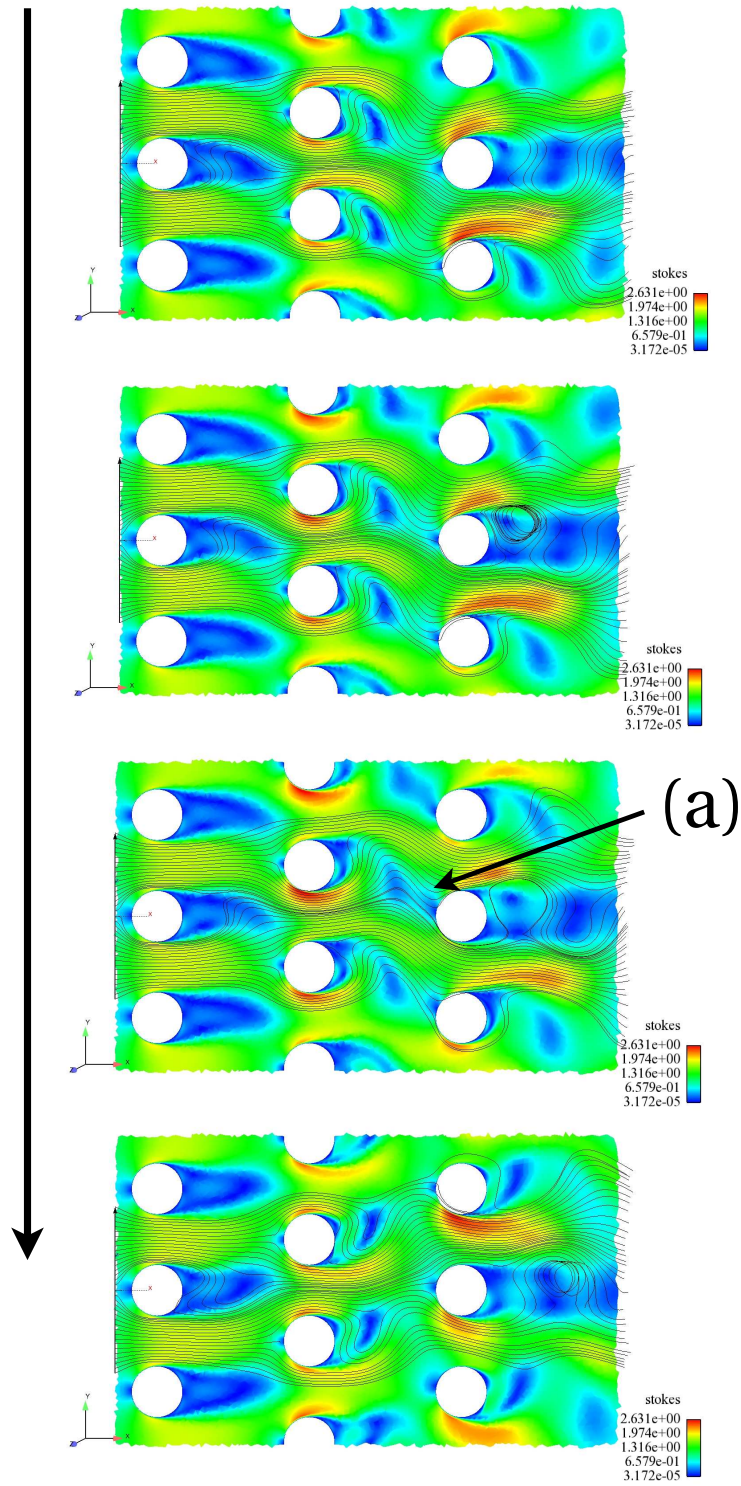


Figure 4.17: Streamline and Stokes number evolution, $U_\infty = 1 \text{ m/s}$, cylinder array, 14 M cells

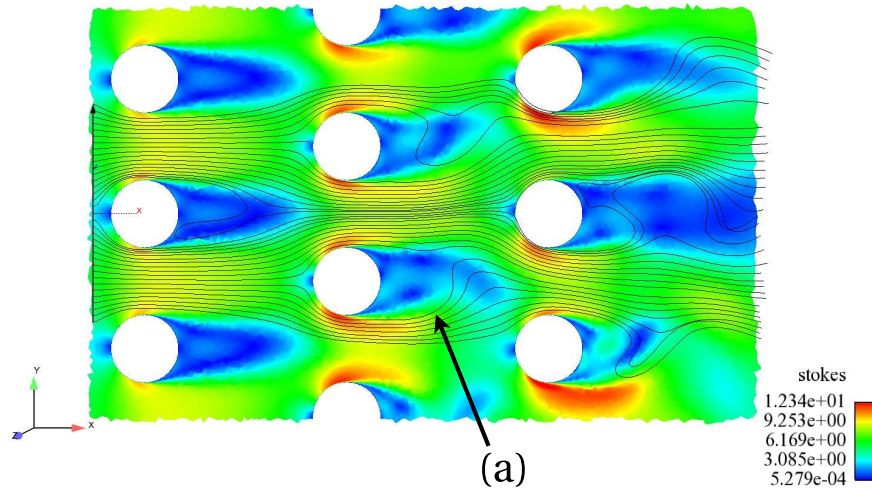


Figure 4.18: Streamline and Stokes number visualization at simulation $t = 3.75 \text{ s}$, $U_\infty = 5 \text{ m/s}$, cylinder array, 14 M cells

through or very near shed vortices where the Stokes number is small. Thus, droplets following these streamlines could easily be entrained inside the vortex and carried along. Animations of the Stokes number, summarized by Figure 4.17, clearly show that vortices shed from the second row of cylinders in the 1 m/s case often directly impact the final row of cylinders. Figure 4.17 (a) points out a vortex shed from Cylinder 2 which impacted Cylinder 3 (Figure 4.7 for cylinder numbers). Naturally, any droplets entrained in a vortex that impacts a cylinder would likely be deposited on the cylinder, accumulate, and drip to the floor.

Conversely, in the 5 m/s free-stream case, shown in Figures 4.18 and 4.19, there are fewer highly curved streamlines in the wake, and those that are present lie in regions of Stokes numbers greater than one (Figure 4.19 (a)), meaning droplets attempting to follow the carrier fluid would fail to negotiate the streamline curvature and instead follow a more ballistic path. Also, in the 5 m/s free-stream case, the animations showed far fewer vortices shed from the second row of cylinders impacting the third row. Thus any droplets that were under the influence of a Karman vortex would not likely be deposited on a cylinder. As a result, fewer droplets in the high speed case would be influenced by the unsteady shedding phenomenon and therefore

Increasing Time

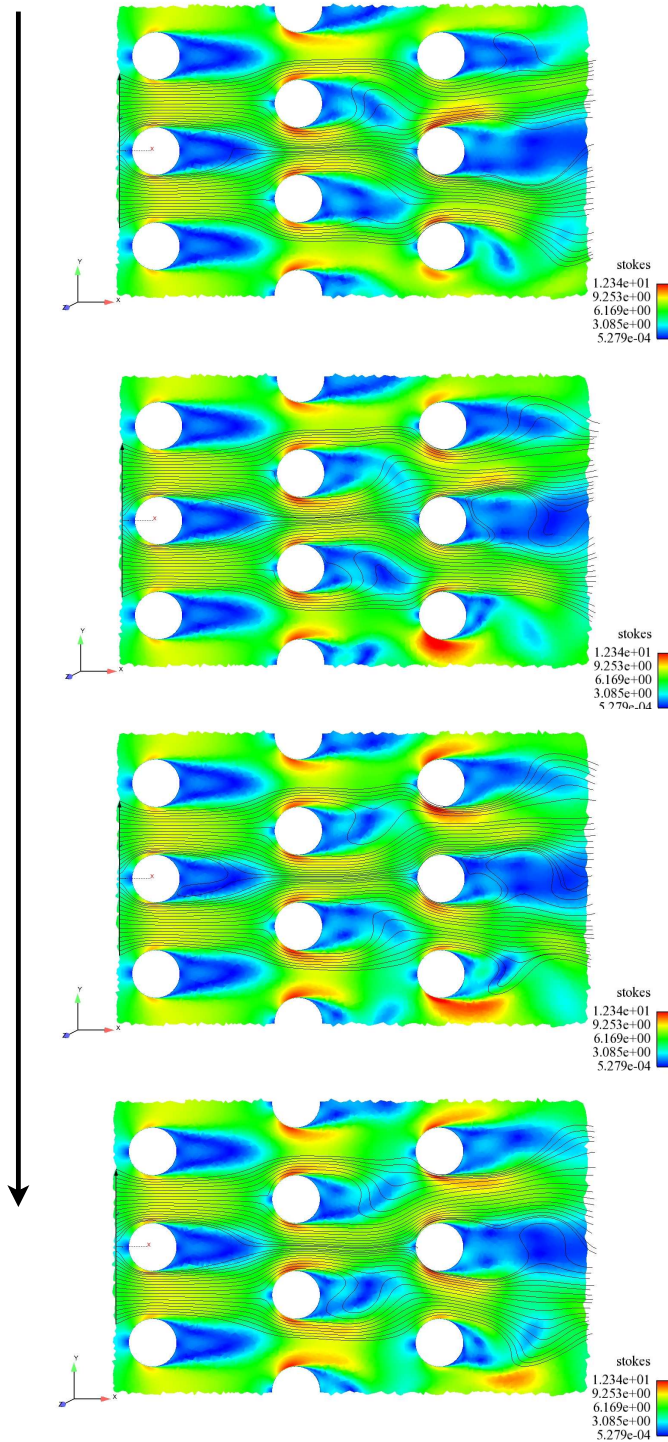


Figure 4.19: Streamline and Stokes number evolution, $U_\infty = 5 \text{ m/s}$, cylinder array, 14 M cells

the motion of entrained droplets will likely be governed primarily by average flow-field characteristics. This, coupled with the transit time analysis of Section 4.3.1, supports the observations of by Disimile et al. [7] and serves as an explanation for the entrapment and transport of droplets inside idealized engine nacelle clutter.

V. Conclusions

Many of the subtleties of CFD and turbulence modeling and analysis were discovered during the process of investigating droplet transport mechanisms through an array of circular cylinders.

5.1 *Detached-Eddy Simulation*

The Detached-Eddy Simulation turbulence modeling technique was successfully demonstrated as an effective tool for computing large turbulent flow structures in low-Reynolds number flows at a relatively modest computational expense when compared with LES. In cases such as the cylinder array, where the unsteady phenomena of interest are large eddies outside of the boundary layer, DES is an excellent numerical method.

The most obvious CFD lesson in this research was stated best by Spalart, “...any unsatisfactory result reported to the author [Spalart] is due to the user’s failure to run on a fine enough grid.” [21] Without a doubt, failure to use a sufficiently refined grid and appropriately small timesteps resulted in poorly resolved transient behavior on the 9.9 million cell grid. Fortunately, the 14 million cell grid, originally only intended as a grid convergence test, adequately captured the bulk shedding phenomenon of the array for both inlet velocity conditions. In the future, more care should be given to spatial/temporal error balancing. The guidance Spalart gives for estimating the time step, $\Delta t = \Delta_0/U_{max}$, discussed in section 2.3.4, should be treated only as an *initial* estimate. The user should experiment freely with space-time balancing and err on the side of small time steps.

5.2 *Droplet Transport*

Two hypotheses were postulated at the outset of this research to explain the droplet transport and entrapment phenomena observed by Disimile et al. [7]. The first hypothesis, which supposed span-wise flow developed in the cylinder wake region due to non-uniform cylinder shedding, was not observed using this model. Instead, this

research successfully demonstrated the veracity of a second hypothesis, which posited the dominance of the velocity-inertia relationship as the governing mechanism for dispersed-phase particles negotiating obstacles.

For slower average velocities inside the array, entrained suppressant droplets will likely fall or be carried into neighboring cylinders before successfully passing through the cylinder array. Conversely, particles entrained in faster flow-fields are able to transit the array before the time required to fall into an obstacle has elapsed. Furthermore, low Stokes number regions capable of capturing entrained droplets were revealed by animations of vortex shedding in the cylinder wake. Vortices that were capable of entraining droplets after shedding from the second row of cylinders often directly collided with the final row of cylinders. Such a collision would certainly deposit the droplets carried by the vortex on the impacted cylinder where the droplets would accumulate and eventually fall to the tunnel floor as super-droplets too large for entrainment.

From the perspective of transporting fire suppressant past bluff body clutter to a downstream fire, high-air-speed flows will clearly be more effective for entraining and transporting suppressant droplets through clutter without impact. However if the cylinders of this research represent fuel lines, the goal of suppressant transport would not be swift conveyance through the array. If one of the fuel lines in the array burst and began spraying fuel into the cylinder wake, a bluff-body stabilized turbulent diffusion flame will form if the fuel were ignited. [1] Under these circumstances, particles dispersed from a suppressant spray nozzle into a high-speed co-flow will not likely reach the cylinder's recirculation region, resulting in a fire that is very difficult if not impossible to extinguish.

5.3 Future Research

Future research regarding the cylinder array should attempt to establish the effect of free-stream turbulence intensity on the flow field inside the cylinder array by using a DES based on a RANS model other than Spalart-Allmaras so that free-

stream disturbances can propagate towards the clutter instead of being damped to zero. Another variable of interest, which was investigated by Disimile et al. [7], was the horizontal cylinder spacing between the rows of cylinders. Disimile et al. logically found that tighter cylinder spacing equated to less droplet transport. However, further investigation of the spacing variable might provide additional insight into the overall droplet transport problem. Finally, a simulation employing *Fluent's*TM dispersed-phase model should be attempted to individually track the particles of the entrained suppressant droplets.

*Fluent*TM is a nominally second-order solver, meaning that the order of the truncation error of the discretization of the governing equations is second-order. Therefore, as the grid is refined and a new solution is computed, the truncation error should decrease by a power of two. Logically, it follows that increased grid refinement is required to reach an acceptably accurate solution for a second-order solver than a higher-order solver. As a result, the requirement of finer meshes for DES in *Fluent*TM increases both the computational and data storage requirements to support the solution. Of course, using a solver with an order of accuracy higher than second-order will likely require using a structured grid to facilitate the larger discretization stencil. Introducing structured grid topology to the problem ushers in a whole new set of obstacles to DES grid generation, however.

The initial condition for a Detached-Eddy Simulation is usually a steady-state RANS solution. Naturally once the DES begins, transient artifacts resulting from the RANS to DES transition will persist in the solution and distort the data. However, the length of time associated with the transients varied more than anticipated from one solution to the next. As a result, computational effort (time) was unnecessarily expended computing and *storing* data which was ultimately discarded. In the future, several seconds of unsteady data should be computed without utilizing the FVE to accelerate obtaining a fully-developed unsteady flow-field.

Finally, demonstrating grid independence of the solution was not accomplished in this study because the fine mesh intended for this purpose was actually the minimum grid resolution necessary to capture the pertinent flow physics. A 25 million cell grid was constructed to meet the needs of the grid convergence study, but the grid could not be exported to *Fluent*TM because *Gridgen*TM, a 32-bit application, was unable to allocate enough memory. If the 25 million cell grid can be exported, the future researchers should be cognoscente of the associate runtime for such a large grid. The average runtime for the 14 million cell grid was 188 hours or 7.9 days to collect two seconds of data when employing the Fluent VTK Extractor (FVE). Based on this, the runtime for the 25 million cell grid will be approximately two weeks to compute two seconds of data.

5.4 Summary

In conclusion, this research modeled the idealized engine nacelle clutter of Disimile et al. in an effort to ascertain flow-field dynamics capable of explaining the failure of water droplets to transit an array of cylinders in low-speed co-flow. Numerical simulations employing Detached-Eddy Simulation were conducted to resolve the turbulent cylinder wakes and examine unsteady flow-field dynamics inside the array. Ultimately, this study determined that droplets emanating from a spray nozzle in co-flow would follow paths governed by the relationship between mean carrier fluid velocities, droplet inertia, and local, unsteady, low-Stokes number regions. For low free-stream velocities (≈ 1 m/s) suppressant droplets will likely become entrained in shed vortices as the droplets pass through low-Stokes number portions of the flow. In the low-speed case, vortices shed from the second row of cylinders typically impacted the third row of cylinders directly; this action would likely deposit any entrained droplets onto the cylinder where they would aggregate and drip. On the other hand, droplets entrained in the higher-speed flow (5 m/s) would not be effected by the carrier fluid's streamlines because the Stokes number in between the cylinders was

substantially higher. Thus, these particles would likely transit the array with ease at mean carrier fluid velocities.

Appendix A. Ancillary CFD Discussions

A few subtleties of CFD are discussed in this section outside of the main document because they do not immediately relate to the overall objective: determining mechanisms of droplet transport inside engine nacelles. However, the information presented here was discovered during the course of the research effort.

A.1 Modified Turbulent Viscosity and Turbulence Intensity

A DES based on the Spalart-Allmaras model cannot adequately transport an elevated level of modified turbulent viscosity from the inlet boundary to the clutter to model the effect of free-stream turbulence and influence separation. This aspect of the Spalart-Allmaras turbulence model is discussed in detail in Section 2.3.2

Because the inlet is $15D$ upstream of the first row of cylinders, the high values of $\tilde{\nu}$ set at the inlet to mimic 10% and 15% turbulence intensity (T.I.) quickly fall back to zero before reaching the clutter. [4, 22] This is clearly evident in Figure A.1 which compares the modified turbulent viscosity level for the 10% and 15% free-stream T.I. cases along a line describing $y, z = 0$ down the length of the single cylinder grid. The cylinder is located at $x = 0$ which explains the absence of $\tilde{\nu}$ values at $x = 0$. For the 15% T.I. curve, the initial values of $\tilde{\nu}$ are only slightly higher than their 10% TI counterparts. In fact, velocity plays a much larger role in elevating $\tilde{\nu}$. Regardless, prior to reaching the cylinder, both cases have been damped to near zero levels.

However, the limitation of the Spalart-Allmaras model should not discourage future researchers from attempting to assess the effect of *accurately* modeled free-stream turbulence intensity. If a DES is employed, then the user should use a k - ϵ or k - ω based DES which would allow the user to input turbulence intensity at the inlet via direct specification of turbulent kinetic energy and the dissipation rate. This option is available in the newest version of *Fluent*TM: 6.3.21. Estimation of the turbulent kinetic energy, k is given by

$$k = \frac{3}{2} (u_{avg} I)^2 \quad (\text{A.1})$$

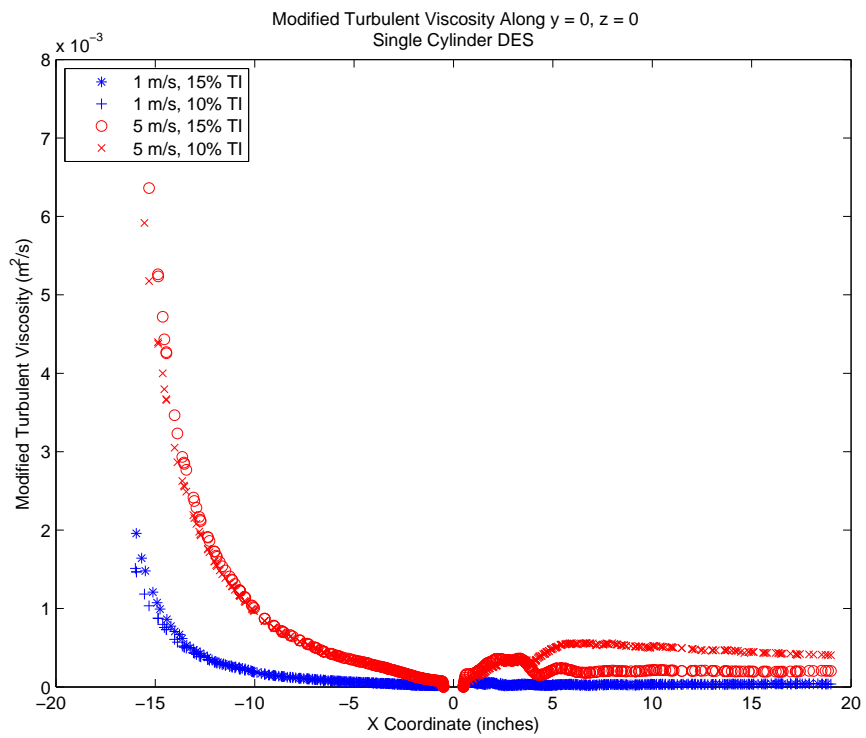


Figure A.1: Modified Turbulent Viscosity, $\tilde{\nu}$, comparison for a single cylinder at 1 m/s .

where I is the turbulence intensity given defined as

$$I = \frac{u'}{u_{avg}} \quad (\text{A.2})$$

and the dissipation rate, ϵ is estimated by

$$\epsilon = C_\mu^{3/4} \left(\frac{k^{3/2}}{l} \right) \quad (\text{A.3})$$

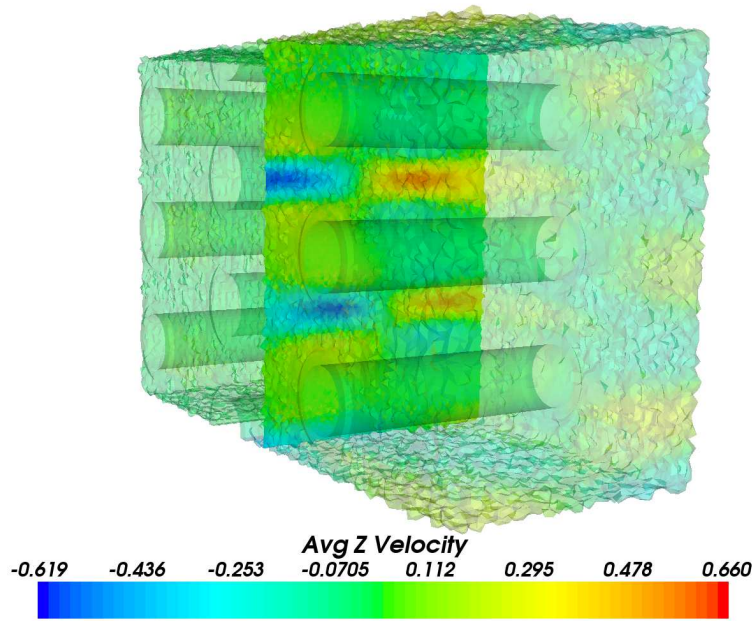
where C_μ is a model constant and l is the characteristic length scale of the turbulence. Alternatively, the dissipation rate can be defined as

$$\omega = \frac{k^{1/2}}{C_\mu^{1/4} l} \quad (\text{A.4})$$

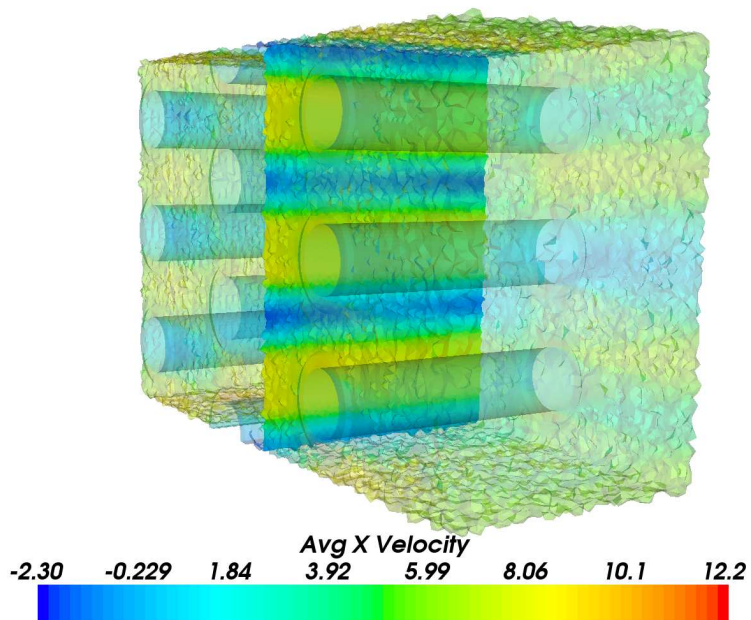
By having two equations describing the transport, generation, and destruction of turbulence, the user will have more control over the level of modified turbulent viscosity reaching the clutter element.

A.2 RANS to DES Transient Artifacts

As noted in Section 5.3, transient artifacts persisted in the DES solution posing as a distracting red herring. Figure ?? depicts regions of positive and negative span-wise velocities with magnitudes upwards of 50% of the local stream-wise velocity in the cylinder wake. This data was collected after well over a second of DES which hinted towards real flow physics. However after running the simulations for three more seconds, these periodic pockets of span-wise flow vanished from the solution.



(a)



(b)

Figure A.2: (a) Average z -velocity (m/s) with $5 m/s$ (14M cells). (b) Average x -velocity (m/s) with $5 m/s$ (14M cells).

Bibliography

1. Anthony, Hamins, Thomas Cleary, Paul Borthwick, Nikolai Gorchkov, Kevin McGrattan, Glenn Forney, and William Grosshandler. “Section 9, Suppression of Engine Nacelle Fires: Fire Suppression System Performance of Alternative Agents in Aircraft Engine and Dry Bay Laboratory Simulations”. *NIST Special Publication 890*, 2, 1995.
2. Barone, Matthew F. and Christopher J. Roy. “Evaluation of Detached Eddy Simulation for Turbulent Wake Applications”. *43rd AIAA Aerospace Sciences Meeting and Exhibit*, AIAA 2005-504. American Institute of Aeronautics and Astronautics (AIAA), Reno, NV, January 2005.
3. Bernard, Peter S. and James M. Wallace. *Turbulent Flow Analysis, Measurement, and Prediction*. John Wiley & Sons, Inc., Hoboken, New Jersey, 2002.
4. Blazek, J. *Computational Fluid Dynamics: Principles and Applications*. Elsevier, New York, 2005.
5. Blevins, R.D. “Forces on and Stability of a Cylinder in a Wake”. *Journal of Off-shore Mechanics and Arctic Engineering-Transactions of the ASME*, 127(1):39–45, 2005.
6. Computational Engineering International, Inc., 2166 N. Salem Street, Suite 101, Apex, NC. *Ensign Users Manual for Version 8.2*, 2006.
7. Disimile, Peter J., James R. Tucker, Brian Crosswell, and John M. Davis. “The Transport of Water Sprays Past Generic Clutter Elements Found Within Engine Nacelles”. *Fire Safety Journal*, 40:65–78, 2005.
8. van Dyke, Milton. *An Album of Fluid Motion*. Parabolic Press, Inc, 1982. Photo by T. Corke, Y. Guezennec, and H. Nagib.
9. Fluent, Inc., Lebanon, NH. *Fluent 6.2 User’s Guide*, 2005.
10. Gann, Richard G. “Next Generation Fire Suppression Technology Program: FY2000 Annual Report”. *NIST Technical Note 1437, National Institute of Standards and Technology*, 2001.
11. Ghee, Terence A. and David R. Keyser. “Basic Aerodynamics Shapes in a Low-Speed, Highly Turbulent Flow”. *21st Applied Aerodynamics Conference*, AIAA 2003-3953. American Institute of Aeronautics and Astronautics (AIAA), Orlando, FL, June 2003.
12. Hassan, Y.A. and H.R. Barsamian. “Tube Bundle Flows with the Large Eddy Simulation Technique in Curvilinear Coordinates”. *International Journal of Heat and Mass Transfer*, 47:3057–3071, 2004.

13. Kolleck, Mathias L., J. Michael Bennett, Jon A. Wheeler, and Gregg M. Caggianelli. *Halon Replacement Program for Aviation: Aircraft Engine Nacelle Application Phase I - Operational Parameters Study*. Technical Report WL-95-3077, Wright Laboratory, Wright-Patterson AFB, Dayton OH, April 1997.
14. Lo, S.-C., K.A. Hoffmann, and J.-F. Dietiker. "Numerical Investigation of High Reynolds Number Flows over Square and Circular Cylinders". *Journal of Thermophysics and Heat Transfer*, 19(1):72–80, January-March 2005.
15. Maple, Raymond C., Ryan Osterday, and Rhonda Vickery. "Fluent VTK Extractor". *Proceedings of the HPCMP Users Group Conference*, 384–388. DoD High Performance Computing Modernization Program, The Institute of Electrical and Electronics Engineers, Inc., Denver, CO, June 2006.
16. Ramachandran, Prabhu. *MayaVi Users Guide*, 2005.
17. "Next Generation Fire Suppression Technology Program: FY2005 Progress". Richard G. Gann (editor), *Halon Options Technical Working Conference, 15th Proceedings*. Building and Fire Research Laboratory, NIST, Gaithersburg, MD, 2005.
18. Roshko, Anatol. *On the Development of Turbulent Wakes from Vortex Streets*. Technical Report Report 1191, California Institute of Technology, National Advisory Committee for Aeronautics, 1958.
19. Sarpkaya, Turgut. "Structures of Separation on a Circular Cylinder in Periodic Flow". *Journal of Fluid Mechanics*, 567:281–297, 2006.
20. Schroeder, William J., Kenneth M. Martin, and William E. Lorensen. *The Design and Implementation Of An Object-Oriented Toolkit For 3D Graphics And Visualization*. Technical report, GE Corporate Research & Development.
21. Spalart, Philippe R. *Young-Person's Guide to Detached-Eddy Simulation Grids*. Technical Report NASA/CR-2001-211032, National Aeronautics and Space Administration, Langley Research Center, Hampton, Virginia, July 2001.
22. Spalart, P.R. and S.R. Allmaras. "A One-Equation Turbulence Model For Aerodynamic Flows". *30th AIAA Aerospace Sciences Meeting and Exhibit*, AIAA 92-0439. American Institute of Aeronautics and Astronautics (AIAA), Reno, NV, January 1992.
23. Spalart, P.R., W-H. Jou, M. Strelets, and S.R. Allmaras. "Comments on the Feasibility of LES for Wings and on a Hybrid RANS/LES Approach". *Advances in DNS/LES, 1st AFOSR International Conference on DNS/LES*. Greyden Press, Columbus, OH, 1997.
24. Tennekes, H. and J.L. Lumley. *A First Course in Turbulence*. The MIT Press, Cambridge, MA, 1972.

25. Travin, Andrei, Michael Shur, Michael Strelets, and Philippe Spalart. “Detached-Eddy Simulations Past a Circular Cylinder”. *Flow, Turbulence and Combustion*, 63:293–313, 1999.
26. Vatsa, Veer N. and Bart A. Singer. “Evaluations of a Second-Order Accurate Navier-Stokes Code for Detached Eddy Simulation Past a Circular Cylinder”. *21st AIAA Applied Aerodynamics Conference*, AIAA 2003-4085. American Institute of Aeronautics and Astronautics (AIAA), Orlando, FL, June 2003.
27. Watterson, J.K., W.N. Dawes, A.M. Savill, and A.J. White. “Predicting Turbulent Flow in a Staggered Tube Bundle”. *International Journal of Heat and Fluid Flow*, 20:581–591, 1999.
28. White, Frank M. *Viscous Fluid Flow*. McGraw-Hill, New York, NY, third edition, 2006.
29. Wilcox, David C. *Turbulence Modeling for CFD*. DCW Industries, Inc., La Cañada, CA, third edition, 2006.

Vita

Matthew Stephen Caspers graduated from General Douglas MacArthur High School in San Antonio, Texas in 1998. He attended Rensselaer Polytechnic Institute in Troy, New York and earned a Bachelors of Science in Aeronautical Engineering. After being commissioned a second lieutenant in the United States Air Force on May 17, 2002, Matthew was assigned to the 82d Aerial Targets Squadron, 53d Weapons Evaluation Group, 53d Wing, Tyndall Air Force Base, Florida. While at Tyndall, he served as the Chief of Engineering presiding over design, fabrication, and flight test of aircraft modifications in support of air-to-air weapons testing. In March 2007, Matthew graduated from the Air Force Institute of Technology with a Masters of Science in Aeronautical Engineering and was selected for the USAF Test Pilot School.

Permanent address: 2950 Hobson Way
Air Force Institute of Technology
Wright-Patterson AFB, OH 45433

REPORT DOCUMENTATION PAGE

Form Approved
OMB No. 0704-0188

The public reporting burden for this collection of information is estimated to average 1 hour per response, including the time for reviewing instructions, searching existing data sources, gathering and maintaining the data needed, and completing and reviewing the collection of information. Send comments regarding this burden estimate or any other aspect of this collection of information, including suggestions for reducing this burden to Department of Defense, Washington Headquarters Services, Directorate for Information Operations and Reports (0704-0188), 1215 Jefferson Davis Highway, Suite 1204, Arlington, VA 22202-4302. Respondents should be aware that notwithstanding any other provision of law, no person shall be subject to any penalty for failing to comply with a collection of information if it does not display a currently valid OMB control number. **PLEASE DO NOT RETURN YOUR FORM TO THE ABOVE ADDRESS.**

1. REPORT DATE (DD-MM-YYYY) 22-03-2007		2. REPORT TYPE Master's Thesis		3. DATES COVERED (From — To) Sept 2005 — Mar 2007	
4. TITLE AND SUBTITLE CFD Investigation of Flow Past Idealized Engine Nacelle Clutter				5a. CONTRACT NUMBER	
				5b. GRANT NUMBER	
				5c. PROGRAM ELEMENT NUMBER	
6. AUTHOR(S) Matthew S. Caspers, Capt, USAF				5d. PROJECT NUMBER	
				5e. TASK NUMBER	
				5f. WORK UNIT NUMBER	
7. PERFORMING ORGANIZATION NAME(S) AND ADDRESS(ES) Air Force Institute of Technology Graduate School of Engineering and Management (AFIT/EN) 2950 Hobson Way WPAFB OH 45433-7765				8. PERFORMING ORGANIZATION REPORT NUMBER AFIT/GAE/ENY/07-M08	
9. SPONSORING / MONITORING AGENCY NAME(S) AND ADDRESS(ES) Dr. Peter J. Disimile 46 TW OG/OGM/OL-AC 2700 D Street Wright-Patterson AFB, OH 45433				10. SPONSOR/MONITOR'S ACRONYM(S)	
12. DISTRIBUTION / AVAILABILITY STATEMENT Approval for public release; distribution is unlimited.				11. SPONSOR/MONITOR'S REPORT NUMBER(S)	
13. SUPPLEMENTARY NOTES					
14. ABSTRACT This research modeled low-speed flow past idealized engine nacelle clutter in support of aircraft fire suppression research. The idealized clutter was comprised of three vertical rows of staggered circular cylinders approximating typical nacelle obstructions such as fuel lines and wire bundles. Single-phase, Detached-Eddy Simulations (DES) were conducted using the commercial CFD solver, <i>Fluent</i> TM , to resolve the flow-field dynamics inside the clutter element and determine mechanisms accounting for the failure of suppressant spray droplets from traversing the array under low-speed, free-stream conditions ($Re_D = 1,575$). The numerical models provided no evidence that span-wise vorticity or non-uniform shedding was responsible for transporting dispersed-phase particles towards the tunnel walls for deposition. However, the simulations demonstrated that suppressant droplets would likely follow a path governed by the vector sum of the local carrier fluid velocity and the velocity imposed by gravity. Additionally, the Stokes number was computed from time-accurate data to determine the ability of dispersed particles to negotiate the clutter element without impinging on a cylinder. For slower free-stream velocities, $U_\infty = 1\text{ m/s}$, suppressant droplets ($D = 90\ \mu\text{m}$) will likely be entrained in vortices shed from the intermediate row of cylinders and subsequently deposited on the last row of cylinders as the Karman vortex directly collides with the clutter. At free-stream velocities, $U_\infty = 5\text{ m/s}$, the droplet particles will likely fail to track the carrier fluid streamlines in the cylinder wake and remain free of any shed vortices. Thus, the suppressant will conceivably transit the cylinder array without impact. These findings imply that a bluff-body turbulent diffusion flame in a cylinder wake could be nearly impossible to extinguish under high-speed, co-flow conditions. Conversely, suppressant transported by low-speed co-flow would experience difficulty traversing the cylinder array and reaching a downstream fire.					
15. SUBJECT TERMS Detached-Eddy Simulation, droplet transport, computational fluid dynamics, array of cylinders, staggered tube bundle, idealized engine nacelle clutter, fire suppression					
16. SECURITY CLASSIFICATION OF:			17. LIMITATION OF ABSTRACT	18. NUMBER OF PAGES	19a. NAME OF RESPONSIBLE PERSON
a. REPORT	b. ABSTRACT	c. THIS PAGE			19b. TELEPHONE NUMBER (include area code)
U	U	U	UU	83	LtCol Raymond C. Maple (937) 255-3636, ext 4577